Nancy-Université
Université
Henri Poincaré

Cursus intégré Saar-Lor-Lux
Physique

DIPLOMARBEIT
RAPPORT DE STAGE M2

Unitary Quench Dynamics of Hard-Core Bosons on a 1D Lattice

Defense: July 5th, 2010 in Nancy, France

Author: Helge Aufderheide
Advisor: Dragi Karevski

Examining Committee:

M.C.	D. Karevski (Nancy-Université, France)	Advisor
Prof.	M. Henkel (Nancy-Université, France)	Examiner
Prof.	M.Y. Choi (Seoul Nat. Univ., S. Korea)	External Examiner
Prof.	S. Heuraux (Nancy-Université, France)	Resp. for the Masters Program
Prof.	B. Kierren (Nancy-Université, France)	Resp. for the Specialization PMC

Version: June 28, 2010

Contents

Part I
Introduction

1 Motivation

The investigation of the movement of objects and the laws behind them have always been one of the main interests of scientific work dating back at least as far as philosophy in ancient Greece [4]. With the development of modern scientific reasoning and technology the field of kinematics is ever changing. From a purely philosophical approach the field of kinetics underwent great changes (advent of Newton's law or quantum dynamics to mention the most prominent.) However, even if the methods get more sophisticated and the objects of research become abstract, the main interest stays the same as narrow or as wide you may define kinematics: Describe the temporal evolution of any given object, may it be a stone from a catapult or the abstract object we call a photon.

In this work we will investigate the dynamics of bosonic particles on a finite one-dimensional chain with a tilted potential. We will later model this situation by the so-called Hubbard model, which was designed originally to describe electrons in low-temperature solid state systems [8]. On one hand, these considerations allow us to understand a wide range of phenomena which might be used in technical applications. Examples are the linking of atomic orbits of a bulk material with those of a substrate, chains of arrays of Josephson junctions [21] or the dynamics of trapped bosonic atoms inside a periodic laser field [9], as well as studies of entanglement [18].

On the other hand the model can easily be reproduced for a wide range of parameters for atoms in laser fields [9] and it has the advantage to be a standard model for Quantum Phase Transitions [5].

2 Formulation of the Problem in Terms of the Bose-Hubbard Hamiltonian

We want to analyze the dynamic behavior of bosonic particles on a a finite chain of L sites (positioned $i = 0, q \ldots L-1$). This system is considered to be governed by the Bose-Hubbard Hamiltonian:

$$\mathbf{H} = \sum_{i=0}^{L-1} \mu_i \mathbf{n_i} + \frac{U}{2} \sum_{i=0}^{L-1} \mathbf{n_i}(\mathbf{n_i} - 1) - \omega \sum_{i,j=0}^{L-1} \left(\mathbf{b_i}^{\dagger} \mathbf{b_j} + \mathbf{b_j}^{\dagger} \mathbf{b_i} \right) \tag{2.1}$$

The first term represents the sum over the energies associated to each site given by the number of particles on the site times the associated chemical potential μ_i. ω is the hopping amplitude between sites i and j whereas U denotes the repulsive two-particle interaction energy if more than one particle occupy a given site (c.f. Figure 1).

The field operators are the bosonic creation and annihilation operators $\mathbf{b_i}, \mathbf{b_i}^{\dagger}$ satisfying the usual commutation algebra $\left[\mathbf{b_i}, \mathbf{b_j}^{\dagger} \right] = \delta_{i,j}$. This system is known to present a Mott-Transition between a superconducting and an isolating phase, the latter one occurring for integer ratios of the total number of particles N and the number of sites L so that we obtain a band structure with

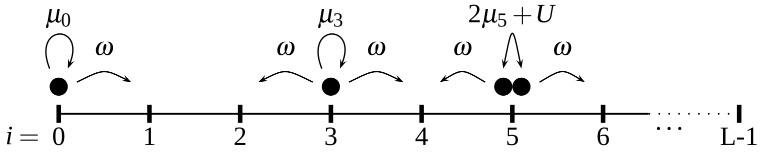

Figure 1: Hopping on the bosonic spin chain with same site interaction Um hopping ω and chemical potential μ_i

energy gaps at $\frac{N}{L}=n, n=0,1,\ldots$. This system has been studied experimentally in the fundamental experiment by Greiner [7] showing the Mott-Insulator phase transition. Also numerical simulations have been carried out with many different generalizations to the model like multiple dimensions [20].

For our work we consider a system at very low temperatures. Therefore, the particle-particle repulsion U is too strong to be overcome by the thermal energy of the particles. If we place ourselves in the first superconducting band $0<\frac{N}{L}<1$ we can send the repulsion of the bosons to infinity. Verifications of the validity of this approximation can be found in [13]. Furthermore we consider jumping between neighboring sites only, breaking down our sum over all combinations of i,j in (2.1) to $i=j\pm 1$.

3 Transformation to free Fermions

3.1 Transformation to the Spin Chain

The description of hard-core bosons as fermions is established in [6]. The system described has only two possible states per site i, occupied $n_i=1$ or non-occupied $n_i=0$, which can be treated analogous to a spin-chain of spins ↑ and ↓. The mapping is established using the following transformation from the bosonic particle creation and annihilation operators to to the spin ladder operators (see [19] for details).

$$\begin{aligned}\sigma_{\mathbf{j}}^{+} &= \mathbf{b_j}^{\dagger}\\ \sigma_{\mathbf{j}}^{-} &= \mathbf{b_j}\end{aligned}$$

which yields

$$\sigma_{\mathbf{j}}^{\mathbf{x}} = \sigma^{+}+\sigma^{-} = \mathbf{b_j}^{\dagger}+\mathbf{b_j} \tag{3.2a}$$

$$\mathrm{i}\sigma_{\mathbf{j}}^{\mathbf{y}} = \sigma^{+}-\sigma^{-} = \mathbf{b_j}^{\dagger}-\mathbf{b_j} \tag{3.2b}$$

$$\sigma_{\mathbf{j}}^{\mathbf{z}} = 2\sigma^{+}\sigma^{-}-\hat{\mathbf{1}} = 2\mathbf{b_j}^{\dagger}\mathbf{b_j}-\hat{\mathbf{1}} \tag{3.2c}$$

Writing the ladder operators in terms of the bosonic creation and annihilation operators $\mathbf{b},\mathbf{b}^{\dagger}$, we recover the common commutation relations of the spin operators (Pauli Matrices) on each site

$$\left[\sigma_{\mathbf{i}}^{\mathbf{j}},\sigma_{\mathbf{i}}^{\mathbf{k}}\right] = 2\mathrm{i}\varepsilon_{jkl}\sigma_{\mathbf{i}}^{\mathbf{l}} \quad j,k,l\in\{x,y,z\}.$$

Inverting (3.2) and inserting in (2.1), we get the Hamiltonian in terms of a spin chain:

$$\mathbf{H} = -\frac{\omega}{2}\sum_{j=0}^{L-1}\left(\sigma_{\mathbf{j}}^{\mathbf{x}}\sigma_{\mathbf{j+1}}^{\mathbf{x}} + \sigma_{\mathbf{j}}^{\mathbf{y}}\sigma_{\mathbf{j+1}}^{\mathbf{y}}\right) + \sum_{i=0}^{L}\frac{\mu_i}{2}\sigma_{\mathbf{j}}^{\mathbf{z}}. \tag{3.3}$$

We have dropped the constant $E_0(N,\mu_i) = \sum_{i=0}^{L-1}\frac{\mu_i}{2}$.

The main advantage of this new formulation of the problem lies in the fact that the spin-chain is a system with well studied dynamics for which a rich set of mathematical tools and results is already available.

Let us briefly review the main properties of the system described by (3.3). For a constant chemical potential, this Hamiltonian is the standard XX-Hamiltonian and is known to present a critical phase transition at $\mu = \frac{\omega}{2}$. For μ higher than this critical value we observe the paramagnetic phase essentially forcing all spins to be aligned with the external field μ. For lower values of μ the system is in a critical fluctuating phase.

The relaxation dynamics in this system have been largely studied (e.g. [2]) as well as the influence of the finite character of the system [3].

3.2 Jordan-Wigner-Transformation to non-interacting Fermions

The Hamiltonian of the XX-Model (3.3) can easily be solved using the Jordan-Wigner Transformation in the case of a translation-invariant potential [12]. For a detailed discussion of the canonical diagonalization see [10, 15–17]. We will proceed analogous to this, but keep in mind the explicitly space-dependent chemical potential μ_i.

The interest of the Jordan-Wigner Transformation is to completely fermionize our system (make the field operators commutation relations those of a system of noninteracting fermions). For the Hamiltonians (3.3) and (2.1) we have commuting operators for different sites, e.g.

$$\left[\sigma_{\mathbf{i}}^{+}, \sigma_{\mathbf{j}}^{-}\right] = 0 \text{ if } i \neq j.$$

For many-body fermionic behavior we need to have an anti-commuting algebra between sites. This expresses that the many-particle wave function is antisymmetric under the exchange of two particles in a fermionic system.

So we need a set of operators mapping from the spin operators σ to the creation and annihilation operators $\mathbf{c}_i^{+}, \mathbf{c}_i$ associated to a given site i.

$$\begin{aligned}\mathbf{c_i} &= \mathbf{A_i}\sigma_{\mathbf{i}}^{-}\\ \mathbf{c_i^{+}} &= \sigma_{\mathbf{i}}^{+}\mathbf{A_i}^{\dagger},\end{aligned}$$

where $\mathbf{A_i}$ is the operator which will be constructed to guarantee the necessary anti-commutation relation, namely

$$\left\{\mathbf{c_i^{+}}, \mathbf{c_j}\right\} = \delta_{i,j} \text{ for all } i, j. \tag{3.5}$$

This implies $\mathbf{A_i}$ to commute with all operators on site i.

$$\left\{\mathbf{c_i}, \mathbf{c_i^{+}}\right\} = \mathbf{A_n}\mathbf{A_n}^{\dagger}\sigma_{\mathbf{i}}^{-}\sigma_{\mathbf{i}}^{+} + \mathbf{A_n}^{\dagger}\mathbf{A_n}\sigma_{\mathbf{i}}^{+}\sigma_{\mathbf{i}}^{-} = \left\{\sigma_{\mathbf{i}}^{-}, \sigma_{\mathbf{i}}^{+}\right\} = \hat{\mathbf{1}}.$$

The actual transformation with the above mentioned properties for the new operators can be shown to be generated by the operator

$$\mathbf{A_n} = \prod_{i<n} (-\sigma_\mathbf{i}^\mathbf{z})\,. \tag{3.6}$$

By taking

$$\sigma_\mathbf{i}^\mathbf{z} = 2\sigma_\mathbf{i}^+\sigma_\mathbf{i}^-\mathbf{1} = 2\mathbf{A_i}^\dagger\mathbf{A_i}\mathbf{c_i^+}\mathbf{c_i} - \mathbf{1} = (\mathbf{c_i^+} + \mathbf{c_i})(\mathbf{c_i^+} - \mathbf{c_i})$$

we can rewrite $\mathbf{A_n}$ in terms of $\mathbf{c}, \mathbf{c}^+$. With this representation of $\mathbf{A_n}$ we express the terms in the Spin-Hamiltonian (3.3) (using (3.5) and the fact that double application of $\mathbf{c_i}$ or $\mathbf{c_i^+}$ is zero):

$$\begin{aligned} \sigma_\mathbf{i}^\mathbf{x}\sigma_\mathbf{i+1}^\mathbf{x} =& (\mathbf{c_i^+} + \mathbf{c_i})(\mathbf{c_i^+} + \mathbf{c_{i+1}}) \\ \sigma_\mathbf{i}^\mathbf{y}\sigma_\mathbf{i+1}^\mathbf{y} =& - (\mathbf{c_i^+} - \mathbf{c_i})(\mathbf{c_i^+} - \mathbf{c_{i+1}}). \end{aligned}$$

It should be noted, that this method only works for a limited set of combinations of the operators $\sigma_\mathbf{i}^\mathbf{k}, k = x,y,z$. In general it creates chains of operators $\mathbf{c_i}\mathbf{c_{i-1}}\ldots$ resulting from the nonlocal character of the operators $\mathbf{c}$.

The transformation applied to our Hamiltonian yields:

$$\mathbf{H} = \sum_{i=0}^{L-1} \mu_i \mathbf{c_i^+}\mathbf{c_i} - \omega \sum_{i=0}^{L-2} \left(\mathbf{c_i}\mathbf{c_{i+1}^+} + \mathbf{c_{i+1}}\mathbf{c_i^+}\right). \tag{3.8}$$

Although the Hamiltonian seems very similar to the bosonic Hamiltonian it now includes the non-local characteristics (creation and annihilations takes into account all particles to the left of the site we are acting upon) of our new operators $\mathbf{c}, \mathbf{c}^+$.

This Hamiltonian can be solved using a simple Bouguliubov-Transformation. For the XX-Hamiltonian ($\mu_i = \mu$) this means essentially Fourier-transforming the annihilation and creation operators.

In our case however, we have to explicitly diagonalize the Hamiltonian to obtain its spectrum and energy eigenmodes generating the transformation.

By introducing the vector

$$\hat{c} = \begin{pmatrix} \mathbf{c_0} \\ \vdots \\ \mathbf{c_{L-1}} \end{pmatrix}$$

$$\hat{c}^+ = \begin{pmatrix} \mathbf{c_0^+} & \cdots & \mathbf{c_{L-1}^+} \end{pmatrix} = \hat{c}^\dagger$$

we can write our Hamiltonian as matrix

$$\hat{\mathbf{H}} = \hat{c}^\dagger \hat{\mathbf{T}} \hat{c}. \tag{3.10}$$

The hermitian matrix $\hat{\mathbf{T}}$ is then

$$\hat{\mathbf{T}} = - \begin{pmatrix} -\mu_0 & \omega & 0 & \cdots & 0 \\ \omega & -\mu_1 & \omega & \ddots & \vdots \\ 0 & \ddots & \ddots & \ddots & 0 \\ \vdots & \ddots & \omega & -\mu_{L-2} & \omega \\ 0 & \cdots & 0 & \omega & -\mu_{L-1} \end{pmatrix}.$$

For any given potential $\mu_i, i = 0..L-1$, we can formally diagonalize the matrix $\hat{\mathbf{T}}$ in order to write the Hamiltonian in a form, that only depends on its one-particle eigenstate creation and destruction operators η_q, η_q^+. Let $\hat{V}_q, q = 1..L$ denote the (normalized) eigenvectors of $\hat{\mathbf{T}}$ of dimension L:

$$\hat{\mathbf{T}}\hat{V}_q = \varepsilon_q \hat{V}_q \quad q = 1..L \tag{3.11}$$

In principle it is then easy to deduce the unitary transformation diagonalizing $\hat{\mathbf{T}}$ to the diagonal matrix $\hat{\mathbf{D}}$:

$$\hat{\mathbf{H}} = \hat{c}^\dagger \hat{\mathbf{D}} \hat{c} = \hat{c}^\dagger \hat{\mathbf{U}} \hat{\mathbf{D}} \hat{\mathbf{U}}^\dagger \hat{c} = \hat{\eta}^\dagger \hat{\mathbf{D}} \hat{\eta}$$

such that

$$\mathbf{H} = \sum_{q=1}^{L} \varepsilon_q \eta^+ \eta.$$

So once this is done, we have the spectrum of the Hamiltonian as well as the operators (η_q^+, η_q)creating or destroying the eigenstate associated to ε_q in the diagonal system. So we can decompose any operator expressed in terms of c, c^+ into its energy eigenmodes and therefore calculate its time-development. Reintroducing the dropped constant from (3.3):

$$\mathbf{H} = \sum_{q=1}^{L} \varepsilon_q \left(\eta^+ \eta - \frac{1}{2} \right). \tag{3.12}$$

3.3 Clifford-Operators

Instead of using (3.10) directly, it is convenient to use a generalized representation in terms of linear combinations of **c** called Clifford operators noted Γ_n^α, where $\alpha = 1, 2$ and n=0..$L-1$. Their definition in terms of the fermionic operators is

$$\Gamma_n^1 = \left(\mathbf{c_i} + \mathbf{c_i}^+ \right)$$
$$\Gamma_n^2 = \mathrm{i} \left(\mathbf{c_i} - \mathbf{c_i}^+ \right).$$

These operators are hermitian by definition and form an algebraic structure called Clifford-Algebra, characterized by $\left\{ \Gamma_n^\mu, \Gamma_m^\nu \right\} = 2\delta_{m,n}\delta_{\mu,\nu}$. The Jordan- Wigner-Transformation then reads [15, 17]:

$$\sigma_\mathbf{i}^\mathbf{x} = \prod_{j<i} (-\mathrm{i}\Gamma_j^2 \Gamma_j^1) \Gamma_i^1 \tag{3.14a}$$

$$\sigma_\mathbf{i}^\mathbf{y} = \prod_{j<i} (-\mathrm{i}\Gamma_j^2 \Gamma_j^1) \Gamma_i^2 \tag{3.14b}$$

$$\text{with } \sigma_\mathbf{i}^\mathbf{z} = -\mathrm{i}\Gamma_i^2 \Gamma_i^1 \tag{3.14c}$$

In this case, we get

$$\sigma_\mathbf{i}^\mathbf{x} \sigma_\mathbf{i+1}^\mathbf{x} = -\,\mathrm{i}\Gamma_i^2 \Gamma_{i+1}^1$$
$$\sigma_\mathbf{i}^\mathbf{y} \sigma_\mathbf{i+1}^\mathbf{y} = -\,\mathrm{i}\Gamma_{i+1}^2 \Gamma_i^1$$

such that

$$\mathbf{H} = \mathrm{i}\frac{\omega}{2}\sum_{j=0}^{L-2}\left(\Gamma^2_j\Gamma^1_{j+1} + \Gamma^2_{j+1}\Gamma^1_j\right) + \mathrm{i}\sum_{j=0}^{L}\frac{\mu_j}{2}\Gamma^2_i\Gamma^1_i. \tag{3.16}$$

which can be symmetrized by substituting $\Gamma^2_i\Gamma^1_j = \frac{1}{2}\left(\Gamma^2_i\Gamma^1_j - \Gamma^1_j\Gamma^2_i\right)$ (we again dropped the constant E_0). As the Hamiltonian is now quadratic in terms of Γ, we introduce the vector

$$\Gamma = \begin{pmatrix} \Gamma_1 \\ \vdots \\ \Gamma_L \\ \Gamma_{L+1} \\ \vdots \\ \Gamma_{2L} \end{pmatrix} = \begin{pmatrix} \Gamma^1_1 \\ \vdots \\ \Gamma^1_L \\ \Gamma^2_1 \\ \vdots \\ \Gamma^2_L \end{pmatrix}. \tag{3.17}$$

and write our Hamiltonian as

$$\hat{\mathbf{H}} = \frac{1}{4}\Gamma^\dagger\hat{\mathbf{T}}\Gamma. \tag{3.18}$$

The hermitian matrix $\hat{\mathbf{T}}$ is in this case given by

$$\hat{\mathbf{T}} = \begin{pmatrix} 0 & \hat{\mathbf{C}} \\ \hat{\mathbf{C}}^\dagger & 0 \end{pmatrix}$$

with

$$\hat{\mathbf{C}} = -\mathrm{i}\begin{pmatrix} -\mu_0 & \omega & 0 & \cdots & 0 \\ \omega & -\mu_1 & \omega & \ddots & \vdots \\ 0 & \ddots & \ddots & \ddots & 0 \\ \vdots & \ddots & \omega & -\mu_{L-2} & \omega \\ 0 & \cdots & 0 & \omega & -\mu_{L-1} \end{pmatrix}.$$

Again, we can for any given potential diagonalize $\hat{\mathbf{T}}$ to write the Hamiltonian in diagonal form with this time $\hat{V_q}$ denoting the (normalized) eigenvectors of $\hat{\mathbf{T}}$ of dimension $2L$:

$$\hat{\mathbf{T}}\hat{V_q} = \varepsilon_q\hat{V_q} \quad q = 1..2L \tag{3.19}$$

So we get for the transformation of $\hat{\mathbf{T}}$ to the diagonal matrix $\hat{\mathbf{D}}$:

$$\hat{\mathbf{H}} = \frac{1}{4}\Gamma^\dagger\hat{\mathbf{T}}\Gamma = \frac{1}{2}\frac{\Gamma^\dagger}{\sqrt{2}}\hat{\mathbf{U}}\hat{\mathbf{D}}\hat{\mathbf{U}}^\dagger\frac{\Gamma}{\sqrt{2}} = \frac{1}{2}\hat{X}^\dagger\hat{\mathbf{D}}\hat{X} \tag{3.20}$$

such that the Hamiltonian reads in terms of the one-particle eigenfunction creation and annihilation operators

$$\mathbf{H} = \frac{1}{2}\sum_{q=0}^{2L}\varepsilon_q\mathbf{X_q}^\dagger\mathbf{X_q}.$$

The factor $\frac{1}{\sqrt{2}}$ in (3.20) guarantees a “normalized” anticommutator $\left\{\mathbf{X_q}^\dagger, \mathbf{X_k}\right\} = \delta_{q,k}$.

We have to find the transformation matrix $\hat{\mathbf{U}}$ (the eigenvectors $\hat{V}_q$ of $\hat{\mathbf{T}}$) to determine the decomposition of any operator in the diagonal system of the Hamiltonian and thus enabling us express its time-development.

It will be useful to rewrite the eigenvectors of the diagonalizing transformation as

$$\hat{V}_q = \frac{1}{\sqrt{2}} \begin{pmatrix} \Phi_q(n=1) \\ \vdots \\ \Phi_q(n=L) \\ -\mathrm{i}\Psi_q(n=1) \\ \vdots \\ -\mathrm{i}\Psi_q(n=L) \end{pmatrix}. \tag{3.21}$$

where the index m in $V_q(m)$ runs over the $2L$ lines. These are basically the Bouguliubov coefficients for the diagonalizing transformation:

$$\mathbf{X_q} = \frac{1}{\sqrt{2}} \sum_{m=1}^{2L} V_q(m)^* \Gamma_m. \tag{3.22}$$

Their inverse yields a result which is totally equivalent to the one we found for the operators $\mathbf{c}, \mathbf{c}^+$ with η_q the annihilation operator of an energy eigenstate:

$$\Gamma_1^m = \sum_q \Phi_q(m) \left(\eta_{\mathbf{q}}^+ + \eta_{\mathbf{q}}\right) \tag{3.23a}$$

$$\Gamma_2^n = \mathrm{i} \sum_q \Psi_q(m) \left(\eta_{\mathbf{q}}^+ - \eta_{\mathbf{q}}\right) \tag{3.23b}$$

$$\mathbf{H} = \sum_q \varepsilon_q \left(\eta_{\mathbf{q}} \eta_{\mathbf{q}}^+ - \frac{1}{2}\right) \quad q = 1 \ldots L \tag{3.23c}$$

This result is for a system without creation and annihilation of particles identical to (3.12) due to a symmetry of the Clifford-operators and Bouguliubov-Coefficients.

To explicitly calculate these coefficients, we use the formulation (3.21) in (3.18) which gives us the two coupled equations (c.f [15])

$$-\mathrm{i}\hat{\mathbf{C}}\hat{\Psi}_q = \varepsilon_q \hat{\Phi}_q \tag{3.24a}$$

$$\mathrm{i}\hat{\mathbf{C}}^\dagger \hat{\Phi}_q = \varepsilon_q \hat{\Psi}_q. \tag{3.24b}$$

These equations allow us to group the solutions for ε_q into a positive and a negative spectrum. From any positive set of solutions $(\hat{\Phi}_q, \hat{\Psi}_q, \varepsilon_q) \quad q = 1..L$ describing a spectrum of particles we can directly deduce its anti-particle counterpart $(-\hat{\Phi}_q, \hat{\Psi}_q, -\varepsilon_q) \quad q = L+1..2L$ and vice-versa. The energy spectrum in terms of $\mathbf{c}, \mathbf{c}^+$ (noted primed) simply neglects the anti-particle spectrum: $\Phi_q(n)' = \Psi_q(n) = \Phi_q(n), \varepsilon_q' = \varepsilon_q \quad q = 1..L$. We will in this work always treat the particle spectrum only and neglect the symmetric antiparticle spectrum.

4 Basic Concepts

After having put forward the problem and simplifications, we will now present the main concepts for its solution including some fundamental results we will need in the course of study.

First of all let us define the basis of our system. The dimension of any complete basis B is 2^L (L independent spins). Each basis is made up from antisymmetric Fock states, each of which describes a combination of L one-spin states ↑ or ↓. Two possible one-spin bases to build up the Fock states from are e.g. the base of localized one-particle-states for the sites i (created/destructed by $\mathbf{c}_i, \mathbf{c}_i^+$) or the eigenstates of the Hamiltonian (associated to $\eta_{\mathbf{q}_i}, \eta_{\mathbf{q}_i}^+$). We can define this latter basis by

$$B = \left\{ |\Psi_{tot}\rangle = \underbrace{\eta_q^+ \eta_{q'}^+ \eta_{q''}^+ \eta_{q'''}^+ \dots}_{\text{all possible combinations of } q\text{'s} \in [1..L]} |0\rangle \right\}.$$

4.1 Conventions

There are some notations and conventions we will use throughout this work. We give a short list of those to keep in mind:

- The Hamiltonian above is over-parametrized. Actually we can factor out ω. Without loss of generality, we can set $\omega = \frac{1}{2}$ and scale μ (and the Energy) in terms of ω.
- We will use the spin $S_i^k \quad k = x, y, z$ which expresses the link of the Pauli Operators σ_i^k with the energy of the expectation values and will be treated analogous to a magnetization. However, as we have set $\hbar = 1$ the difference between the operators is merely formal. The expectation value for S^k is taken to range from -1 (associated to $|\downarrow\rangle$) to 1 ($|\uparrow\rangle$), where -1 is a non-occupied and 1 an occupied state in terms of bosonic particles.
- We sometimes substitute the integer variable denoting the position by a continuous variable. In this case, we will no longer refer to the position with variables canonically denoting integers (e.g. n, m, i) but by a variable associated to a continuous position (e.g. x, y, z). We will then use the magnetization $m^k(x)$ and the particle density $\rho(x)$ instead of the spins on each site S_i^k. In general we will use subscript indices like μ_i to denote discrete dependencies. To avoid confusion with multiple indices, a notation analogous to the continuous system is sometimes used also for the discrete case (thus e.g. $\mu(i)$) .
- The connection between the spin and the bosonic operators is given by

  $$n_i = \frac{1}{2}(S_i^z + 1)$$

  or in the continuous case

  $$\rho(x) = \frac{1}{2}(m_k^z(x) + 1).$$

- The Heaviside step function is denoted by

$$\Theta(x) = \begin{cases} 0 & \text{if} \quad x < 0 \\ 1 & \text{if} \quad x \geq 0 \end{cases}$$

and the door (formally boxcar) function

$$\sqcap\!\sqcap(a \ldots b; x) = \begin{cases} 1 & \text{if} \quad a \leq x \leq b \\ 0 & \text{otherwise} \end{cases} . \tag{4.1}$$

4.2 Expectation Values, Wicks Theorem and Representation in Terms of the Correlation Matrix

Our interest lies mainly in the expectation values of observables, like the energy $\langle \mathbf{H} \rangle = E$ or the spin at a given position $\langle \sigma_{\mathbf{i}}^{\mathbf{z}} \rangle$.

In general we have:

$$\langle \mathbf{O} \rangle = \mathrm{Tr}\left\{ \mathbf{O} \rho \right\},$$

where ρ represents the density matrix operator and the trace being taken over any complete basis.

We have shown, that all degrees of freedom are those of the spins for all sites. Changing into the energy eigensystem they can always be expressed in terms of the Clifford Operators (3.14a)(3.14b) (3.14c).

Wicks theorem states, that it is always possible to factorize these expectation values of many-operator products down to a sum of products of two-operator expectation values. If we know the behavior of all two-operator expectation values, we can formally deduce the expectation value of any physical observable. In our case these two-operator expectation values are:

$$\langle \Gamma_n^\mu \Gamma_m^\nu \rangle \quad \mu, \nu = 1,2 \quad n, m = 0 \ldots L-1,$$

basically the correlators between the Clifford-Operators associated to sites n and m according to their values. These correlators (prefixed by $-\mathrm{i}$ to create a real matrix) can be written in a matrix form called correlation matrix:

$$\hat{\mathbf{G}} = -\mathrm{i} \begin{pmatrix} \left\langle \Gamma_0^1 \Gamma_0^1 \right\rangle & \cdots & \left\langle \Gamma_1^1 \Gamma_{L-1}^1 \right\rangle & \left\langle \Gamma_0^1 \Gamma_0^2 \right\rangle & \cdots & \left\langle \Gamma_0^1 \Gamma_{L-1}^2 \right\rangle \\ \vdots & \cdots & \vdots & \vdots & \cdots & \vdots \\ \left\langle \Gamma_{L-1}^1 \Gamma_0^1 \right\rangle & \cdots & \left\langle \Gamma_{L-1}^1 \Gamma_{L-1}^1 \right\rangle & \left\langle \Gamma_{L-1}^1 \Gamma_0^2 \right\rangle & \cdots & \left\langle \Gamma_{L-1}^1 \Gamma_{L-1}^2 \right\rangle \\ \left\langle \Gamma_0^2 \Gamma_0^1 \right\rangle & \cdots & \left\langle \Gamma_0^2 \Gamma_{L-1}^1 \right\rangle & \left\langle \Gamma_0^2 \Gamma_0^2 \right\rangle & \cdots & \left\langle \Gamma_0^2 \Gamma_{L-1}^2 \right\rangle \\ \vdots & \cdots & \vdots & \vdots & \cdots & \vdots \\ \left\langle \Gamma_{L-1}^2 \Gamma_0^1 \right\rangle & \cdots & \left\langle \Gamma_{L-1}^2 \Gamma_{L-1}^1 \right\rangle & \left\langle \Gamma_{L-1}^2 \Gamma_0^2 \right\rangle & \cdots & \left\langle \Gamma_{L-1}^2 \Gamma_{L-1}^2 \right\rangle \end{pmatrix}$$

which can be written as

$$\hat{\mathbf{G}} = \begin{pmatrix} \hat{\mathbf{M}}_{\mathbf{1}} & \hat{\mathbf{I}} \\ -\hat{\mathbf{I}} & \hat{\mathbf{M}}_{\mathbf{2}} \end{pmatrix}.$$

$\hat{\mathbf{M}_{\mathbf{1},\mathbf{2}}}$ are unknown matrices and

$$I_{i,j} = -\mathrm{i} \left\langle \Gamma_i^1 \Gamma_j^2 \right\rangle.$$

Notice that

$$I_{i,i} = \langle \sigma^z \rangle.$$

4.3 Thermal States

Let us determine $\hat{\mathbf{G}}$ for an equilibrium state at temperature T. Let β be the inverse temperature and η_q, η_q^+ the creation/annihilation operators of the diagonalized Hamiltonian eigenstates. We have to calculate for the expectation value of any operator

$$\langle \mathbf{O} \rangle = \mathrm{Tr}\left\{\mathbf{O}\rho\right\} \quad \rho = \frac{\mathrm{e}^{-\beta \sum_{q''} \varepsilon_{q''} \left(\eta_{q''}^+ \eta_{q''} - \frac{1}{2}\right)}}{Z},$$

where Z represents the partition function

$$Z = \mathrm{Tr}\left\{ \mathrm{e}^{-\beta \sum_{q''} \varepsilon_{q''} \left(\eta_{q''}^+ \eta_{q''} - \frac{1}{2}\right)} \right\} = \prod_{q''} \cosh\left(\beta \frac{\varepsilon_{q''}}{2}\right).$$

By introducing (3.23a)(3.23b) and then using the orthogonality of the eigenstates in the eigenbasis of the Hamiltonian as well as those of $\Phi_q(n), \Psi_q(n)$ (with $\eta_q^+ \eta + \eta_q \eta_q^+ = \mathbf{1}$) yields [16]

$$\begin{aligned}
(M_s)_{n,m} &= -\mathrm{i}\left\langle \Gamma_n^s \Gamma_m^s \right\rangle \\
&= \mathop{\mathrm{Tr}}_{1\ldots L} \left\{ \sum_{q,q'} \left(\eta_q^+ + \eta_q\right) \left(\eta_{q'}^+ + \eta_{q'}\right) \Phi_q(n) \Psi_{q'}(m) \rho \right\} \\
&= -\mathrm{i} \sum_{q,q'} \delta_{q,q'} \Phi_q(m) \Psi_q(n) = -\mathrm{i}\delta_{n,m} && (4.2) \\
I_{n,m} &= -\mathrm{i}\left\langle \Gamma_n^1 \Gamma_m^2 \right\rangle \\
&= \sum_q \mathop{\mathrm{Tr}}_{1\ldots L} \left\{ \left(\eta_q^+ \eta_q - \eta_q \eta_q^+\right) \Phi_q(n) \Psi_q(m) \frac{\prod_{q''} \mathrm{e}^{-\beta \varepsilon_{q''} \left(\eta_{q''}^+ \eta_{q''} - \frac{1}{2}\right)}}{Z} \right\} \\
&= \sum_q \mathop{\mathrm{Tr}}_{\substack{1\ldots q-1,\\ q+1\ldots L}} \left\{\sim\right\} \otimes \mathop{\mathrm{Tr}}_q \left\{\sim\right\} \\
&= -\sum_q \Phi_q(n) \Psi_q(m) \frac{\mathrm{Tr}_{\substack{1\ldots q-1,\\ q+1\ldots L}} \left\{\sim\right\}}{\mathrm{Tr}_{\substack{1\ldots q-1,\\ q+1\ldots L}} \left\{\sim\right\}} \frac{\left(\mathrm{e}^{\frac{\beta}{2}\varepsilon_q} - \mathrm{e}^{-\frac{\beta}{2}\varepsilon_q}\right)}{\cosh\left(\frac{\beta}{2}\varepsilon_{q''}\right)} \\
&= -\sum_q \Phi_q(n) \Psi_q(m) \tanh\left(\frac{\beta}{2}\varepsilon_q\right). && (4.3)
\end{aligned}$$

such that

$$\hat{\mathbf{G}} = \begin{pmatrix} 0 & \hat{\mathbf{I}} \\ -\hat{\mathbf{I}} & 0 \end{pmatrix} - \mathrm{i}\hat{\mathbf{1}}.$$

4.4 Unitary Dynamics of the Correlation Matrix

The time evolution of the system is done as described in the proceedings in [14, 15]. In the Heisenberg picture

$$\mathbf{O}(t) = \mathbf{U}_\mathbf{t}'^\dagger(t) \mathbf{O}(0) \mathbf{U}_\mathbf{t}'(t),$$

where $\mathbf{U}_\mathbf{t}' = \mathrm{e}^{-\mathrm{i}\mathbf{H}t}$ is the the time evolution operator.

The time evolution on the non-observable diagonal operators of the Hamiltonian $\mathbf{X}_q$ as defined in (3.22) is given by [15]

$$\begin{pmatrix} X_q(t) \\ X_q^\dagger(t) \end{pmatrix} = \begin{pmatrix} \mathrm{e}^{-\mathrm{i}\varepsilon_q t} & 0 \\ 0 & \mathrm{e}^{\mathrm{i}\varepsilon_q t} \end{pmatrix} \begin{pmatrix} X_q \\ X_q^\dagger \end{pmatrix}$$

Therefore we get in terms of the Clifford operators ($\hat{\mathbf{U}}$ is the diagonalizing transformation):

$$\begin{aligned} \Gamma(t) =& \sqrt{2}\hat{\mathbf{U}}\hat{X}(t) \\ =& \underbrace{\sqrt{2}\hat{\mathbf{U}}\exp\left(-\mathrm{i}\hat{\mathbf{D}}t\right)\frac{1}{\sqrt{2}}\hat{\mathbf{U}}^\dagger}_{\hat{\mathbf{R}}(t)}\Gamma(0) \\ =& \mathrm{e}^{-\mathrm{i}\hat{\mathbf{T}}t}\Gamma(0), \end{aligned}$$

where

$$\hat{\mathbf{R}} = \mathrm{e}^{-\mathrm{i}\hat{\mathbf{T}}t}$$

is unitary. We see from the above equations, that its elements are

$$R_n^m = \sum_{q=1}^{2L} V_q(n)V_q^*(m)\mathrm{e}^{-\mathrm{i}\varepsilon_q t} \tag{4.4}$$

which can be simplified considering the symmetry of the energy spectrum for $\varepsilon \to -\varepsilon$. With $n,m \in [0, L-1]$:

$$\begin{aligned} R_n^m &= \sum_{q=1}^{L} \Phi_q(n)\Phi_q(m)\cos(\varepsilon_q t) \\ R_n^{m+L} = -R_{n+L}^m &= \sum_{q=1}^{L} \Phi_q(n)\Psi_q(m)\sin(\varepsilon_q t) \\ R_{n+L}^{m+L} &= \sum_{q=1}^{L} \Psi_q(n)\Psi_q(m)\cos(\varepsilon_q t). \end{aligned}$$

The time evolution of the expectation values of arbitrary operators can be calculated using the dynamics of $\hat{\mathbf{G}}$. The connection to the dynamics of the Cliffor-Operators is readily made:

$$(G(t))_{i,j} = \left\langle -\mathrm{i}\Gamma_i](t)\Gamma_j^\dagger(t)\right\rangle = \sum_{i,j} R_k^i(t)\left\langle -\mathrm{i}\Gamma_i(0)\Gamma_j^\dagger(0)\right\rangle R(t)_j^{*l} = \sum_{i,j} R_k^i(t)\,(G(0))_{k,l}\,R(t)_j^l$$

yielding the final result

$$\mathbf{G}\hat{(\mathbf{t})} = \mathbf{R}\hat{(\mathbf{t})}\mathbf{G}\hat{(\mathbf{0})}\mathbf{R}\hat{(\mathbf{t})}^\dagger. \tag{4.6}$$

In principle this allows us via Wicks theorem to calculate any observable in the system at any given time t from the initial correlation matrix.

4.5 Conserved Quantities

To get a rough idea of basic constraints of the dynamics in our system,we study its conserved quantities. The first is obviously the total energy, which is always conserved if the Hamiltonian has no explicit time dependence because of

$$\frac{\mathrm{d}\,\mathbf{H}}{\mathrm{d}t} = \mathrm{i}\,[\mathbf{H},\mathbf{H}] + \frac{\partial\,\mathbf{H}}{\partial t}.$$

We can define a kinetic and potential energy

$$E_{pot} = \sum_{i=0}^{L-1} \left(\frac{\mu_i}{2}\right) \langle \mathbf{S_i^z} \rangle \tag{4.7a}$$

$$E_{kin} = \left(-\frac{\omega}{2}\right) \sum_{i=0}^{L-2} \left(\langle \mathbf{S_i^x S_{i+1}^x} \rangle + \langle \mathbf{S_i^y S_{i+1}^y} \rangle\right) \tag{4.7b}$$

$$E_{tot} = \langle \mathbf{H} \rangle = E_{pot} + E_{kin}.$$

The second conserved quantity is the total magnetization or equivalently the total number of particles.

$$\langle \mathbf{S_{tot}^z} \rangle = \sum_{i=0}^{L} \langle \mathbf{S_i^z} \rangle = 2N_{tot} - L.$$

This value, not depending on the change of the potential at $t = 0$ is obviously conserved due to

$$\begin{aligned}
\frac{\mathrm{d}\,\mathbf{S_{tot}^z}}{\mathrm{d}t} =& -\mathrm{i}\left[\mathbf{H}, \sum_i \mathbf{S_i^z}\right] \\
=& \frac{\omega}{2}\left[\sum_i \mathbf{S_i^z}, \sum_{i=0}^{L-2} \left(\mathbf{S_i^x S_{i+1}^x} + \mathbf{S_i^y S_{i+1}^y}\right)\right] \\
=& \frac{\omega}{2}\sum_{i=0}^{L-2} \left(2\mathrm{i}\left(\mathbf{S_i^y S_{i+1}^x} + \mathbf{S_i^x S_{i+1}^y}\right) - 2\mathrm{i}\left(\mathbf{S_i^x S_{i+1}^y} + \mathbf{S_i^y S_{i+1}^x}\right)\right) \\
=& 0.
\end{aligned}$$

Part II
Quench Dynamics

5 Quench Protocol

The protocol of our simulations will be to create a localized initial state in thermal equilibrium and then abruptly changing the underlying potential. According to recent experiments [9] at low temperatures we set $T = 0$. The initial state at $t = 0$ is created using a potential of the form of a well causing condensation of all particles inside this part of the system. The position and density profile of the condensate can be controlled by the potential. In general we will trap the particles in an area next to the left border of the system.

At $t = 0+$, we abruptly change the potential profile. Therefore the initial state is no longer the ground state of the new system and we observe non-equilibrium dynamics.

In Figure 2 we show a draft of the two situations at $t = 0$ and $t > 0$.

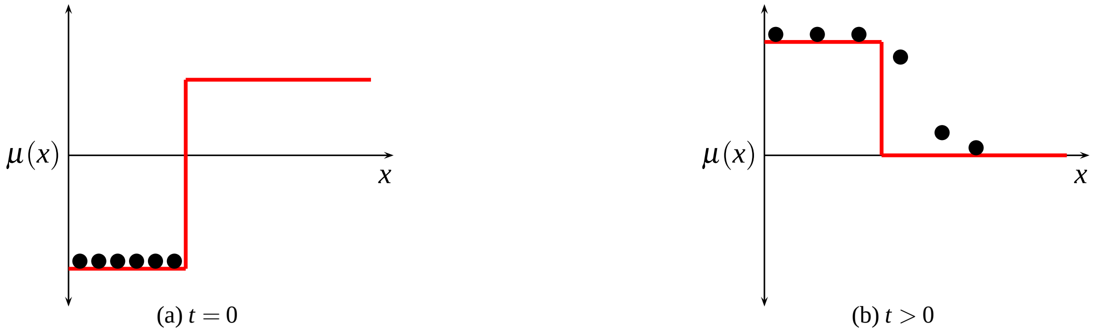

(a) $t = 0$ (b) $t > 0$

Figure 2: Schema of the quench protocol for an inverse well as final potential.

It should be noted that this relaxation dynamics is unitary (no dissipation, E_{tot} conserved) and conserves the number of particles.

6 Initial State

Let us characterize the initial state shown in Figure 2.

The first step is to find the Hamiltonian eigenstates. We can treat the problem of diagonalizing the Hamiltonian in analogy with a potential well problem although the interpretation of our eigenfunctions as coefficients for creation and annihilation operators in the framework of second quantization is different.

6.1 Eigenstates and Energy Spectrum

The initial state is created inside a flat potential well of constant potential localized in a left part of width A of the system of total length L. For now, we suppose to have infinite walls to expel particles from any other region.

$$\mu_i = \begin{cases} \mu_0 & \text{for} \quad 0 \le i < A \\ \mu_R \to \infty & \text{for} \quad A \le i < L \end{cases}.$$

To find the spectrum of this system on the chain we solve (3.24a),(3.24b) with the Ansatz

$$\Phi(i) = \Psi(i) = \exp(\pm \mathrm{i} q(i+\delta)), \tag{6.1}$$

where δ is a phase angle to be determined by the boundary conditions. Using the boundary conditions

$$\Phi(-1) = \Phi(A) = 0, \tag{6.2}$$

we get a quantization of energy (and q). The final states associated to a given energy ε_k are linear combinations of (6.1) associated to q_k and $-q_k$. Noting the final states by $\Phi_k(i)$, we finally get (similar to a continous square well):

$$\varepsilon_k = \mu_0 - 2\omega \cos(q_k) \tag{6.3}$$

$$\Phi_k(i) = \Psi_k(i) = \tilde{A} \sin((i+1)q_k) \tag{6.4}$$

with $\tilde{A} = \sqrt{\frac{2}{A}}$ the normalization constant and

$$q_k = \frac{k\pi}{A+1}, k = 1 \dots A.$$

Note that from now on we will set $\omega = \frac{1}{2}$, to simplify the dispersion relation (6.3). Furthermore we will define for a given site i the potential and kinetic energy corresponding to an energy eigenmode k by fixing:

$$E_{potk} = \mu_i \quad \text{and} \quad E_{kink} = -\cos(q_k). \tag{6.5}$$

6.2 Thermal initial State

As mentioned in 4.3, we can describe the system in thermal equilibrium by the correlation matrix:

$$\left(\hat{\mathbf{I}}\right)_{n,m} = -\sum_k^L \Phi_k(n)\Psi_k(m) \tanh\left(\frac{\beta}{2}\varepsilon_k\right). \tag{6.6}$$

For zero temperature

$$\tanh(\frac{\beta}{2}\varepsilon_q) = \mathrm{sign}(\frac{\beta}{2}\varepsilon_k) = \mathrm{sign}(\varepsilon_k). \tag{6.7}$$

We have to distinguish the well-known critical and non-critical regions of the XX-Model. For $|\mu_0| > 1$ (paramagnetic phase), all ε_k are of same sign, such that

$$\left(\hat{\mathbf{I}}\right)_{n,m} = -\delta_{n,m} \mathrm{sign}(\varepsilon_n).$$

$$S_z = -\mathrm{sign}(\varepsilon) \tag{6.8}$$

is always directed against the external field. In terms of bosonic occupation density:

$$\rho = \frac{1}{2}(-\mathrm{sign}(\varepsilon)+1).$$

If $|\mu_0| < 1$, part of the spectrum ε_k is positive and part of it is negative. We have namely N occupied states $0 < q_k \leq q_N$ with $q_N = \max\{q, q_k < -\arccos(\mu_0)\}$. Using (6.6) to calculate S_i^z yields

$$\left(\hat{\mathbf{I}}\right)_{i,i} \approx -\frac{2}{\pi}\arcsin(\mu_0) \tag{6.9a}$$

$$+\frac{2\cos(i\arccos(\mu_0))}{A}+\frac{2\cos(\frac{i\pi}{A})\sin(\frac{i\pi}{A})\cos(i\arccos(\mu_0))\cos(i\arccos(\mu_0))}{A(1-\cos(\frac{i\pi}{A}))}, \tag{6.9b}$$

where we have neglected terms in higher than second order of $\frac{\pi}{A}$. (6.9a) is the usual result for the critical system. (6.9b) is vanishing with distance from the border and system size and therefore merely a finite size effect.

A similar approximation to the values for the off-diagonal elements of $\hat{\mathbf{I}}$ results in

$$\begin{aligned}\left(\hat{\mathbf{I}}\right)_{n,m} \approx & \frac{2}{A}\sin(m\arccos(\mu_0))\sin(n\arccos(\mu_0)) \\ & +\left(\frac{2}{A}\sin(m\arccos(\mu_A))\cos(n\arccos(\mu_0))\sin(\frac{n\pi}{A})\right. \\ & \left.-\frac{2}{A}\cos(m\arccos(\mu_0))\sin(n\arccos(\mu_0))\sin(\frac{m\pi}{A})\right)\frac{1}{\cos(\frac{n\pi}{A})-\cos(\frac{m\pi}{A})}.\end{aligned}$$

Again we have a volume term vanishing with the size of the system. In addition to that we have the correlation term between nearby sites, which decreases with growing $m-n$.

As an example we consider the simple case $\mu_0 = 0$. This will also serve to show the phenomenological difference between a system with infinite walls and the case, in which the potential stays finite for $i \geq A$.

In the infinite well case, we have to solve

$$S_z = \frac{1}{L}\sum_k \mathrm{sign}(\frac{\beta}{2}\varepsilon_k)$$

which is zero due to the symmetry of $\cos(q_k)$ around $q = \pi/2$. There are exactly half of all states with positive and half of them with a negative spin, so they cancel out because of

$$\sin\left(n\frac{\pi}{L+1}\right) = \sin\left((L+1-n)\frac{\pi}{L+1}\right).$$

Now we try to understand how non-vanishing boundary conditions at A change this situation. On one hand the above mentioned symmetry of q is broken. An easy calculation can be done to approximately model this for $\mu_0 = 0$. We take the eigenfunctions of the infinite case as reference

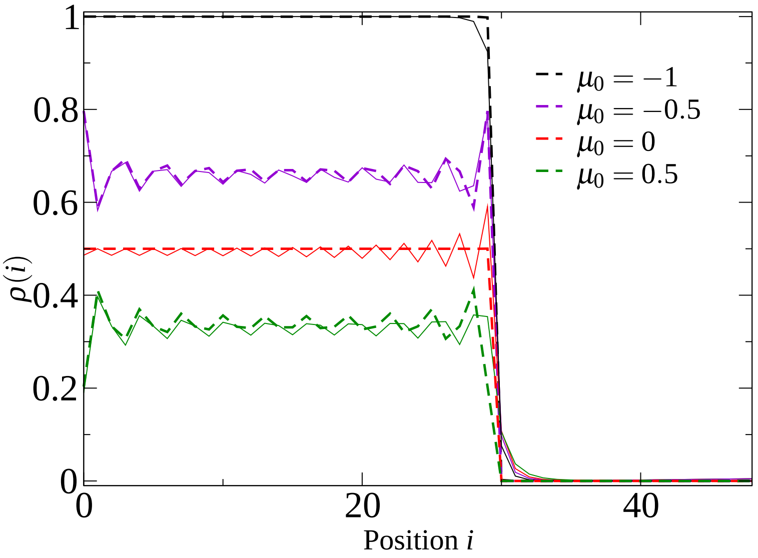

Figure 3: Results for the initial occupation density created by different initial potentials μ_0 for a system of $A = 30$ with $\omega = 1/2$. For $i \geq 30$ the system continues with an infinite (dashed lines) or finite ($\mu_0 = 1$, straight lines) potential.

but use a simple small constant shift to the wave vector $q_0 = k\frac{\pi}{A+1} + \delta$. Then we can extract approximately inside the system of length A from (6.6) :

$$I_{n,n} = -\left(1 - 2\delta n \cot\left(\pi \frac{n}{M+1}\right)\right) \begin{cases} \sin\left(\frac{\pi n}{2(M+1)}\right) & \text{if } n \text{ even} \\ \cos\left(\frac{\pi n}{2(M+1)}\right) & \text{if } n \text{ odd} \end{cases} .$$

This introduces oscillations of unit wavelength far from the boundary and diverges near the boundary as observed in the numerical data.

For other values of μ_0 this effect is masked by the oscillations of finite sum over the eigenfunctions, that canceled out for $\mu_0 = 0$ due to the symmetry of q. Numeric results are shown in Figure 3 alongside with the initial densities created using different initial values for μ_0.

A reasonable approximation of the initial occupation density is according to (6.9) in the continous limit given by

$$\rho(x) = \frac{\alpha}{\pi}\Theta(A - x) \quad \alpha = \arccos(-\mu_0). \tag{6.11}$$

7 Dynamics of the Step Potential

So far we have only considered the properties of our system at a given time $t = 0$, creating thermal states and calculating expectation values. We will now turn to the dynamics for $t > 0$ as described in 5. First we will treat the very simple step system as a starting point to understand the fundamental laws underlying the time-evolution of the particle density.

We are using the Heisenberg picture, so our initial state remains time-independent, while we apply an evolution to the operators and thus their expectation values. We will proceed by diagonalizing the Hamiltonian before putting forward the main characteristics of the dynamics. Let our system be described by a step function chemical potential on site i:

$$\mu_i = \begin{cases} \mu_A & \text{for} \quad 0 \leq i < A \\ \mu_B & \text{for} \quad A \leq i < L \end{cases}.$$

7.1 Dispersion Relation and Energy Spectrum

We now solve (3.11) or analogously the system (3.24a),(3.24b).

Separating the system into System A ($0 \leq i < A$) and B ($A \leq i < L$), we can solve it inside each of them with the same Ansatz (6.1) as we did for the initial potential in 6.1. Inside each of the two systems the dispersion relation reads

$$\varepsilon = \mu_K - \cos(q_K) \quad K = A, B. \tag{7.1}$$

Therefore we have, when looking at the two systems together for any given energy ε_k:

$$\varepsilon_k = \begin{cases} \mu_A - 2\omega\cos(q_{Ak}) \text{ in region A} \\ \mu_B - 2\omega\cos(q_{Bk}) \text{ in region B} \end{cases} \tag{7.2}$$

with the constraint

$$\mu_A - \mu_B = \cos(q_{Bk}) - \cos(q_{Ak}) \tag{7.3}$$

Combining this with the boundary conditions in $i = -1, A, L$ we will obtain a discretization of the L possible energy values $\varepsilon_k, k = 1 \ldots L$ associated to compatible pairs of wave vectors q_{Ak}, q_{Bk}.

7.1.1 Boundary Conditions at 0 and $L-1$ and A

From the vanishing boundary conditions at $n = -1, L$ we get (using the Ansatz (6.1) inside Systems A and B separately) and using the dispersion relation:

$$\begin{aligned} \Phi_A(n) = \Psi_A(n) =& \tilde{A}\sin(q_A(x+1)) \\ \Phi_B(n) = \Psi_B(n) =& \tilde{B}\sin(q_B(x-L)). \end{aligned}$$

$\tilde{A}, \tilde{B}$ are normalization constants. To quantize the energy ε_k and identify the associated compatible wavenumbers q_{Ak}, q_{Bk} we go ahead and plug these into the boundary conditions at the interface between A and B (resulting from (3.11)). Together with the constraint (7.3) we have to solve

$$\begin{aligned} \left(\sin(q_A(A-1)) + \frac{\tilde{B}}{\tilde{A}}\sin(q_B(A-L))\right) + (-\mu_A + \varepsilon)\sin(q_A A) =& 0 \\ \left(\frac{\tilde{A}}{\tilde{B}}\sin(q_A A) + \sin(q_B(A+1-L))\right) + (-\mu_B + \varepsilon)\sin(q_B(A-L)) =& 0. \\ \cos(q_B) - \cos(q_A) =& \mu_A - \mu_B \end{aligned}$$

This leaves us (after elimination of the quotient of the normalization constants and ε by the dispersion relation) with the system :

$$\begin{aligned} \sin(q_B(A-L))\sin(q_A A) = \sin(q_A(A+1))\sin(q_B(A-1-L)) \\ \mu_A - \mu_B = cos(q_B) - \cos(q_A) \end{aligned}$$

The $k = 1 \ldots L$ solutions (q_{Ak}, q_{Bk}) to this system are nontrivial.

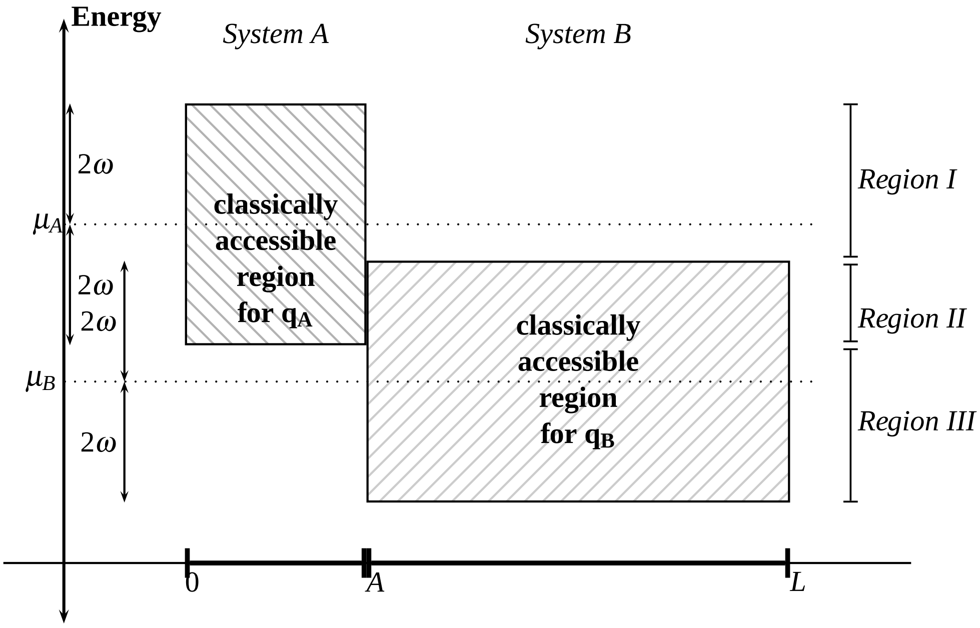

Figure 4: Schematic draft of the energetically accessible regions. Treating electrons and holes will add the mirrored spectrum to the shown picture which is associated to $\varepsilon \to -\varepsilon$. As those spectra are totally independent due to the symmetry stated above we limit our considerations to one of them.

7.1.2 Allowed Energy Regions

Although we cannot calculate the solutions for q_A and q_B exactly, a closer look at (7.2) reveals, that q_A and q_B have imaginary parts for $\left|\varepsilon_k - \mu_{A/B}\right| > 1$, changing the eigenfunction sinus to a hyperbolic sinus decrease. We will therefore call a spacial region accessible for a state of given energy ε_k if it's wavenumber q_k is real inside this region, such that the state shows oscillatory behavior. In the same way we will call states of imaginary wavenumber forbidden. Note that every state has to be allowed inside at least one Subsystem A or B to allow normalization. Assuming $\mu_A > \mu_B$, we can therefore define three energy ranges. All states inside each of them have the same allowed and forbidden spacial regions:

Region I $\mu_A + 1 > \varepsilon_k > \mu_B + 1$, $\Phi_k(i)$ is allowed inside $0 \ldots A-1$, q_{Ak} is real, $q_{Bk} = \pi + \mathrm{i}q'_{Bk}$ causing decreasing oscillations inside the forbidden region.

Region II $\mu_B + 1 > \varepsilon_k > \mu_A - 1$, $\Phi_k(i)$ is allowed inside $0 \ldots L-1$, q_{Ak} and q_{Bk} are real.

Region III $\mu_A - 1 > \varepsilon_k > \mu_B - 1$, $\Phi_k(i)$ is allowed inside $A \ldots L-1$, $q_{Ak} = \mathrm{i}q'_{Ak}$ is imaginary, q_{Bk} is real.

In Figure 4 those regions are sketched. It is important to note, that the region II may disappear if $|\mu_A - \mu_B| > 2$, leaving Regions I and III as two energetically decoupled systems.

We limit our considerations to the case $\mu_B \leq \mu_A$, the other case can be directly deduced by symmetry.

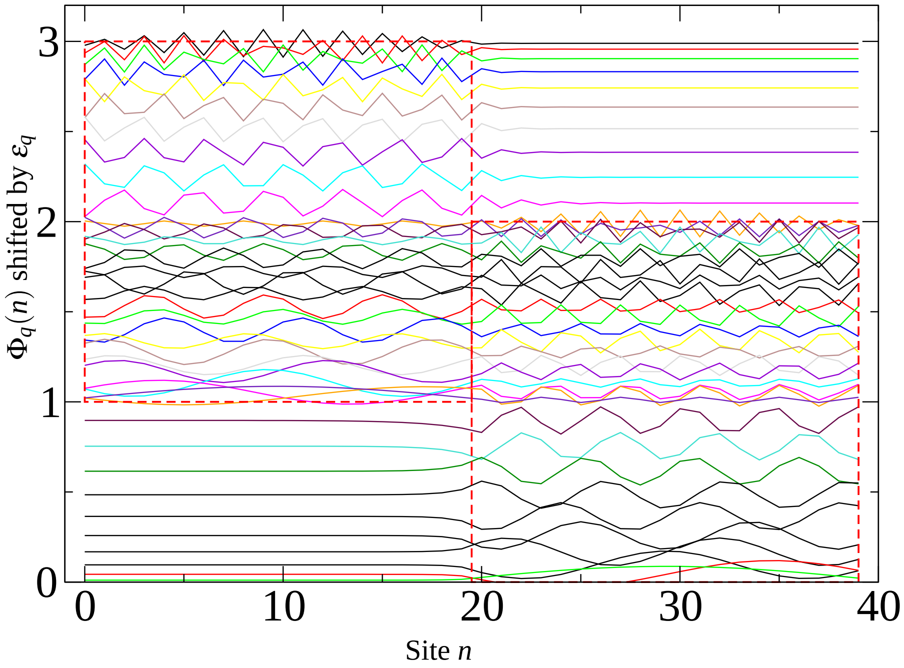

Figure 5: $\Phi_q(n) (= \Psi_q(n))$ shifted by their associated energy Eigenvalues for a system of $L = 40$ sites using $A = 20$ $mu_A = 2$, $mu_B = 1$, $\omega = 0.5$. The dashed line represents the borders of the allowed energy regions

The structure of our solutions will be as follows if we start with $\mu_A - \mu_B = 0$ and gradually increase the potential difference: First we see only modes spanning the whole length of the system with $q_{Ak} = q_{Bk} = \pi \frac{N}{L+1}, N = 1 \ldots L$. Slight increases do not change the picture but shift the energy levels. Increasing further, the upper- and lowermost energy levels drop one after another into regions I or III resp. until we are left with the two decoupled systems at $\mu_A - \mu_B > 2$.

The eigenfunctions of the Hamiltonian are shown in Figure 5 for an example potential difference of $\mu_A - \mu_B = 1$.

We see clearly the three regions described above as well as the increasing number of nodes if we move up in Energy.

7.2 Density of States

It will often be interesting to pass into the continuum limit in ε_k

$$\sum_k f(\varepsilon_k) \to \int \mathrm{d}\varepsilon\, n(\varepsilon) f(\varepsilon).$$

using the density of states $n(\varepsilon) = \frac{1}{\varepsilon_{k+1} - \varepsilon_k}$. Let us determine the total density of states from the density of states of the two simple systems.

For systems A and B separately we can define a density of states in terms of wavenumbers

$n(q_K), K = A, B$ from what we have seen so far:

$$n_A(q_A) = \frac{A}{\pi} \lceil\rceil(0 \dots \pi; q_A) \quad \text{and} \quad n_B(q_B) = \frac{L-A}{\pi} \lceil\rceil(0 \dots \pi; q_B) \tag{7.5}$$

leading (via (6.3)) to

$$n_K(\varepsilon) = \frac{n_K(q_K)}{\sqrt{1-(\varepsilon-\mu_K)^2}} \lceil\rceil(\mu_K - 1 \dots \mu_K + 1; \varepsilon), \quad K = A, B.$$

Let us recall the Hamiltonian (3.16). If we define the two Subsystem Hamiltonians $\mathbf{H}_K$, $K = A, B$ as the part of the Hamiltonian acting only on subsystem A or B, we can rewrite

$$\mathbf{H} = \mathbf{H}_A + \mathbf{H}_B + \mathrm{i}\frac{\omega}{2}\left(\Gamma^2_{A-1}\Gamma^1_A + \Gamma^2_A\Gamma^1_{A-1}\right) = \mathbf{H}_A + \mathbf{H}_B + \mathbf{H}_{mix}.$$

allowing to approximate

$$\frac{\langle \mathbf{H}_{mix} \rangle}{\langle \mathbf{H}_A \rangle} \approx \frac{1}{A} \ll 1 \quad \text{and} \quad \frac{\langle \mathbf{H}_{mix} \rangle}{\langle \mathbf{H}_B \rangle} \approx \frac{1}{L-A} \ll 1.$$

Therefore we can expect the energy spectrum $\operatorname{spect}\mathbf{H_K}$ to be very little changed by the contribution of the interacting part $\mathbf{H}_{mix}$. If we are now interested in the spectrum of the total Hamiltonian, it will therefore approximately be the superposition of the two initial spectra that stay almost unchanged:

$$\operatorname{spect}\mathbf{H} \approx \operatorname{spect}\mathbf{H}_A \bigoplus \operatorname{spect}\mathbf{H_B} \tag{7.6}$$

As a consequence, the density of states for the complete system is the sum of the two initial ones:

$$n(\varepsilon) \approx n_A(\varepsilon) + n_B(\varepsilon) = \frac{A\lceil\rceil(\mu_A - 1 \dots \mu_A + 1; \varepsilon)}{\pi\sqrt{1-(\varepsilon-\mu_A)^2}} + \frac{(L-A)\lceil\rceil(\mu_B - 1 \dots \mu_B + 1; \varepsilon)}{\pi\sqrt{1-(\varepsilon-\mu_B)^2}} \tag{7.7}$$

The results for a relatively big ratio of A to $L - A$ is shown in Figure 6. We can see, that the mean of the numerically found density of states $n(\varepsilon) = \frac{1}{\varepsilon_{k+1}-\varepsilon_k}$ is very well modeled by (7.7). The superposition can qualitatively also be seen in Figure 5.

Actually we can make a similar development for the wave numbers q. Their value inside one subsystem of length can only be shifted by a maximum of $\pm\frac{\pi}{2l}$ by the linking of the two subsystems. This is due to the fact, that the number of zeros of a given state associated to ε_k is fixed to $k - 1$ and has therefore to stay unchanged inside each of the systems, such that finally $q_k \in [\frac{(k+\frac{1}{2})\pi}{l+1}, \frac{(k-\frac{1}{2})\pi}{l+1}]$.

7.3 Velocity of Excitations on the Chain

A fundamental quantity of our Hamiltonian is the propagation velocity of excitations on the chain. For the uniform initial state with an abrupt change of magnetization resp. particle density, we expect to see an excitation dynamic starting from this interface point.

The dispersion relation (7.2) suggests to characterize the propagation of this perturbation by a propagation velocity:

$$v_k = \frac{\mathrm{d}\,\varepsilon_k}{\mathrm{d}q_k} = \sin(q_k) \quad \Rightarrow \quad 0 < |v| < 1 \tag{7.8}$$

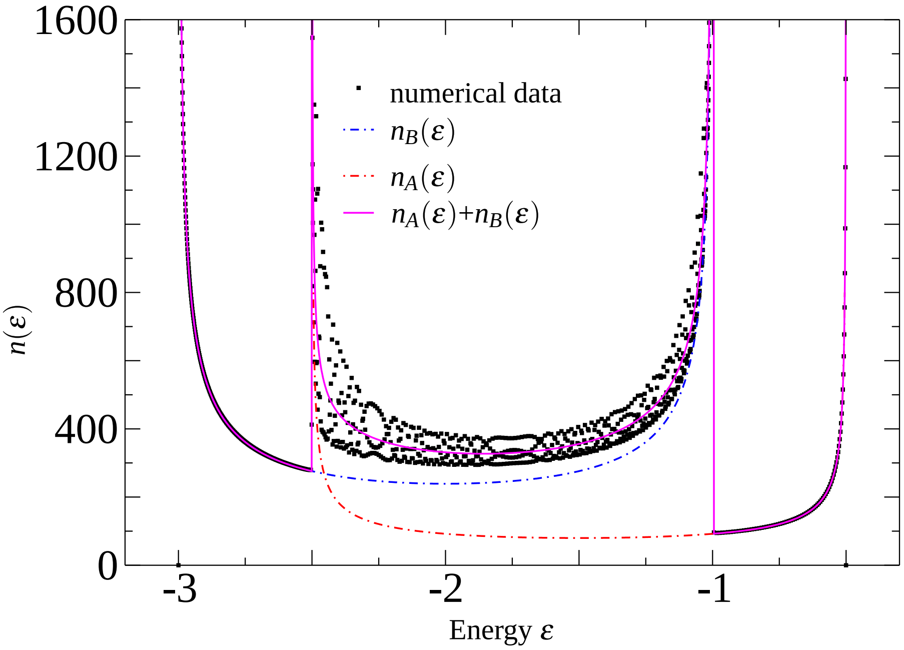

Figure 6: Density of states obtained numerically and by the approximation of a linear distribution of states $n_{A/B}(q)$ inside Systems A and B with parameters $\omega = 0.5$, $\mu_A = -1.5$, $\mu_B = -2$ $L = 1000$ $A = 250$.

The maximum velocity $c = 1$ limits the propagation of any perturbation of our system.

Physically it means, that our system is locally in equilibrium outside of $|x| > ct$ as created at $t = 0$ just until the perturbation has reached it. Any site $|x| < ct$ will be influenced by the initial perturbation. In other words a causal relation between two events on our chain can only exist, if the distance between the two events is smaller than ct.

The propagation speed associated to a certain energy ε_k at position i is then defined by:

$$v_k = \sin(q_k) = \pm\sqrt{1 - (\varepsilon_k - \mu_i)^2}$$

So propagation is fastest for $\varepsilon_k = \mu_i$ and slowest at the maximum and minimum of the allowed energy regions $\varepsilon_k = \mu_i \pm 1$.

7.4 Time-Evolution of the Magnetization Profile

7.4.1 Flat XX-Model System (Greens Function Approach)

We will demonstrate in a first step the dynamics on the well-studied and simple to understand XX-Model ($\mu_i = \mu = Const.$), for which it is actually possible to calculate the time-evolution explicitly in terms of Bessel functions. For this case, the chemical potential is uniform, so we expect a linear propagation of any perturbation. In our case we suppose to prepare the system with a magnetization according to

$$m^z(x) = (\alpha+1)\Theta(A-x) - 1 \quad \alpha = -1\dots 1, \tag{7.9}$$

where $\Theta(x)$ denotes the Heaviside step function.

As the new equilibrium state at $t \to \infty$ will be the uniform distribution of particles over the whole chain, we expect a propagation of magnetization to the right and demagnetization to the left. The conservation of total spin and the symmetry of our initial state suggest, that these two excitations will propagate completely symmetrical in different directions until their symmetry is broken due to the finite size of our system, when they hit a wall. The maximum speed of propagation will of course be $v \leq c = 1$.

In this special case of a flat final potential it is possible to describe the development of $\langle S^z \rangle (n)$ by a discrete convolution product of the initial magnetization and a Greens function. The explicit result including the form of the Greens function can be found in the discrete and continous case [15, 17].

$$\langle S_i^z(t)) \rangle = F_0(t) \star \left\langle S_p^z(0) \right\rangle = \sum_k F(n-k) \left\langle S_p^z(0)) \right\rangle$$

In the continous case the Greens function and convolution are

$$m^z(x,t) = \int_{-\infty}^{\infty} \mathrm{d}y\, F_0(y,t) m^z(x-y,0) \tag{7.10}$$

with the Greens function

$$F_0(y,t) = \frac{1}{t} f\left(\frac{x}{t}\right) \tag{7.11}$$

$$f(v) = \begin{cases} \frac{1}{\pi}\left(1-v^2\right)^{-\frac{1}{2}} & \text{if} \quad |v| < c = 1 \\ 0 & \text{if} \quad |v| > c = 1 \end{cases}$$

For the initial step magnetization (7.9) we get for the magnetization as long as it has not reached the walls of our system

$$m^z(x,t) = \begin{cases} \alpha & \text{if} \quad x < A - ct \\ \frac{\alpha-1}{2} - \frac{\alpha+1}{\pi} \arctan\left(\frac{x}{\sqrt{t^2-x^2}}\right) & \text{if} \quad A - ct \leq x \leq A + ct\ . \\ -1 & \text{if} \quad A + ct < x \end{cases} \tag{7.12}$$

These results do not depend on the actual value of the constant field.

It is interesting to note that this relation takes a scaling form in $v = \frac{x}{t}$.

The solutions of this approach are represented together with the numerical results for a chain system in Figure 7, yielding an excellent agreement if we neglect the small oscillations caused by the quantum character of the system.

We observe that the numeric data agrees with the results from the Greens function as long as we have not met a system boundary with our propagating excitation. The propagation occurs with a maximum speed of $c = 1$ in agreement with the previous paragraph. So the first change of behavior can be seen for a system of 30 sites at about $t^* = 30$, when the left front hits the left

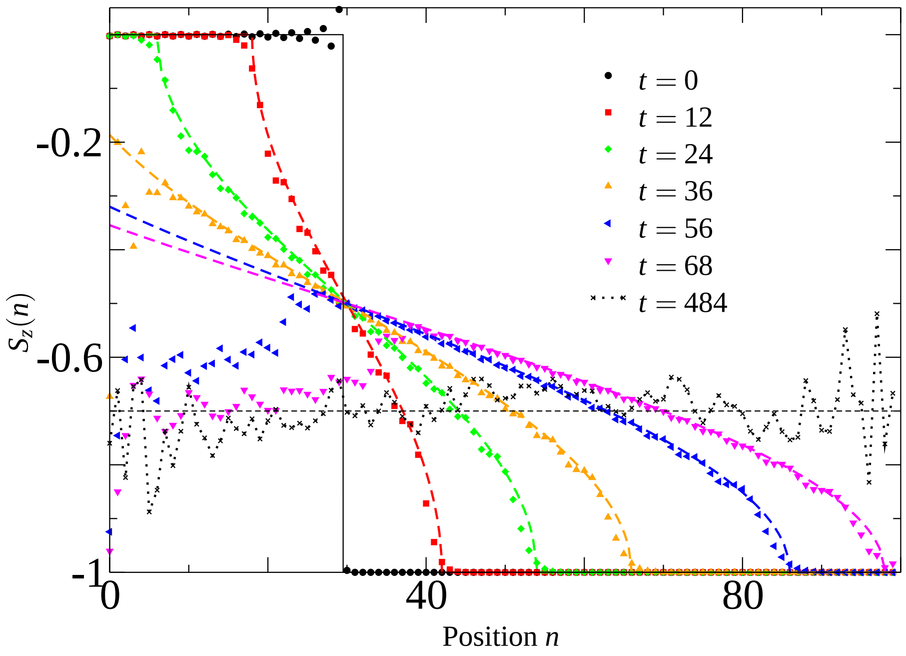

Figure 7: Time-dependent results for $A = 30$ initially at zero temperature with $\alpha = 0$ in a flat potential ($\mu = 0$). Numerical results (symbols) and their continuum solutions (corresponding dashed graphs, solid black for initial state) for different times. The dashed vertical line marks the theoretical final distribution at $S_z = -0.7$ and can be seen as the theoretical curve for $t \to \infty$

wall and is reflected and moves back to the right. The obvious symmetry in A of the problem so far reflects spin conservation.

For long times (not shown in this graph) we observe an interference of the positive and negative wave packages being reflected by the two walls and widening more and more while approaching the new equilibrium distribution shown in Figure 7.

7.4.2 Step System

In the step-potential we expect a far richer dynamics than for the XX-System, because of the two distinct spectra of the two sides of the system. As a first step towards a description of the dynamics we will show and analyze the phenomenology of the time-evolution of this system for the well-known thermal state localized to the left for different final potentials.

The graphs in Figure 8 show the evolution of $S^z(n)$ for different final potentials. Let us recall the Hamiltonian

$$\mathbf{H} = -\frac{\omega}{2}\sum_{j=0}^{L-1}\left(\sigma_{\mathbf{j}}^{\mathbf{x}}\sigma_{\mathbf{j+1}}^{\mathbf{x}} + \sigma_{\mathbf{j}}^{\mathbf{y}}\sigma_{\mathbf{j+1}}^{\mathbf{y}}\right) - \sum_{i=0}^{L}\frac{\mu_i}{2}\sigma_{\mathbf{j}}^{\mathbf{z}}.$$

A negative μ means favoring positive spin in the according region, while positive μ disfavors them. As an example let us use the initial magnetizations as created by an initial $\mu_0 = 0$ or -8 corresponding to a half and complete filled initial system.

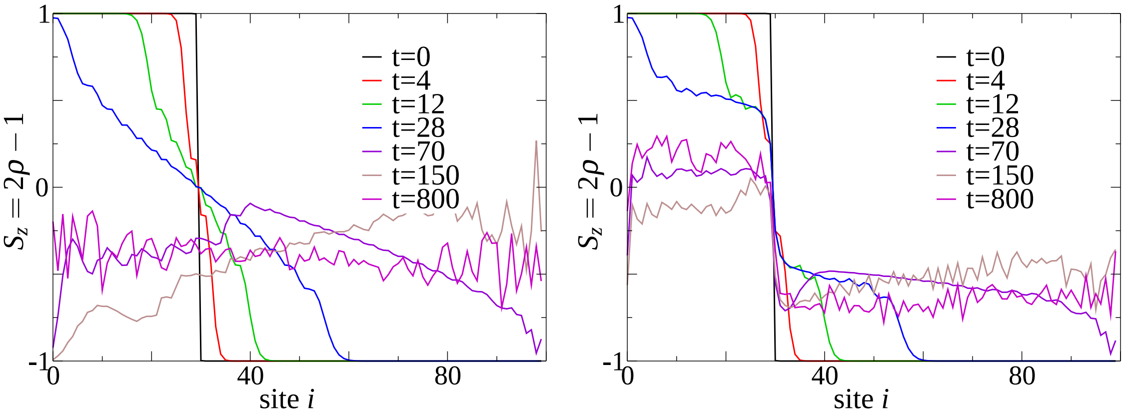

(a) $\mu_A = 0$ (b) $\mu_A = 0.5$

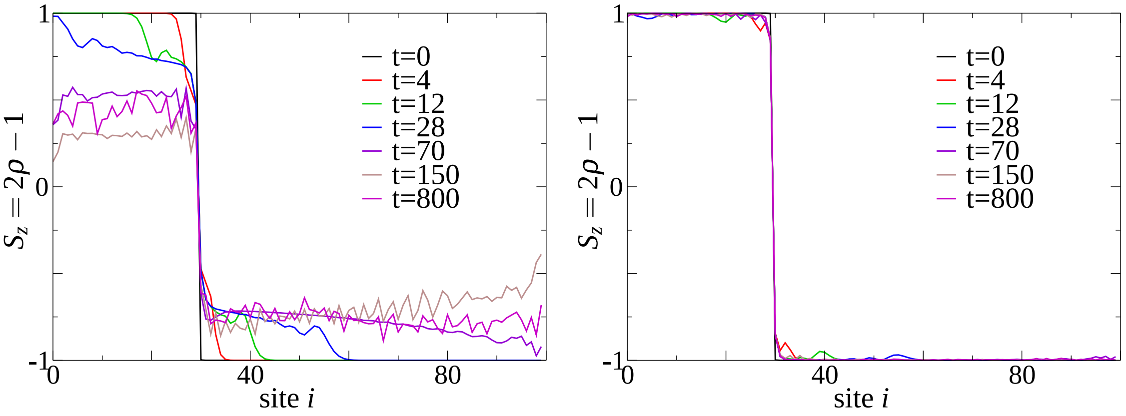

(c) $\mu_A = 1$ (d) $\mu_A = 2$

Figure 8: S_i^z at different points in time for different final potential μ_A. $\mu_B = 0$. Initially we filled the system with $\mu_0 = -8$, corresponding to complete filling for $A = 30$, $L = 100$

The results for the development under $\mu_B = 0 < \mu_A$ for a completely filled initial reservoir at $t = 0$ are mainly the following: We see the situation for a final uniform potential (as in section 7.4.1) being a symmetric perturbation spreading to both sides of the barrier until the wall of the system is reached when a pattern of waves reflected by the walls is created. For other values of $\mu_A < 2$ we observe the same phenomenology, but with increasing the potential difference, the moving perturbation gets smaller, leaving more and more the central part of the initial boundary at A intact.

Let us now look at the case of an only partially filled reservoir at $t = 0$. The results can be found in Figure 9. We again observe a similar evolution of the magnetization, but the symmetry for small times around A is lost for all but the flat potential case.

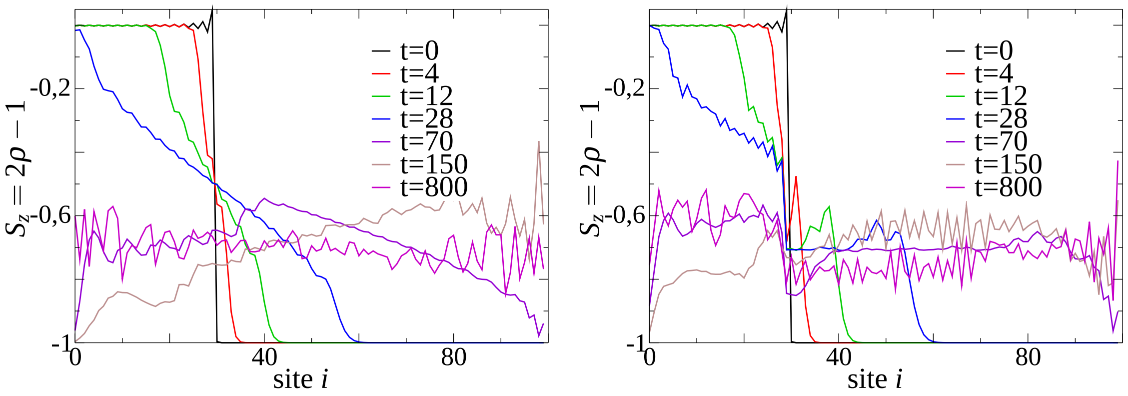

(a) $\mu_A = 0$ (b) $\mu_A = 0.5$

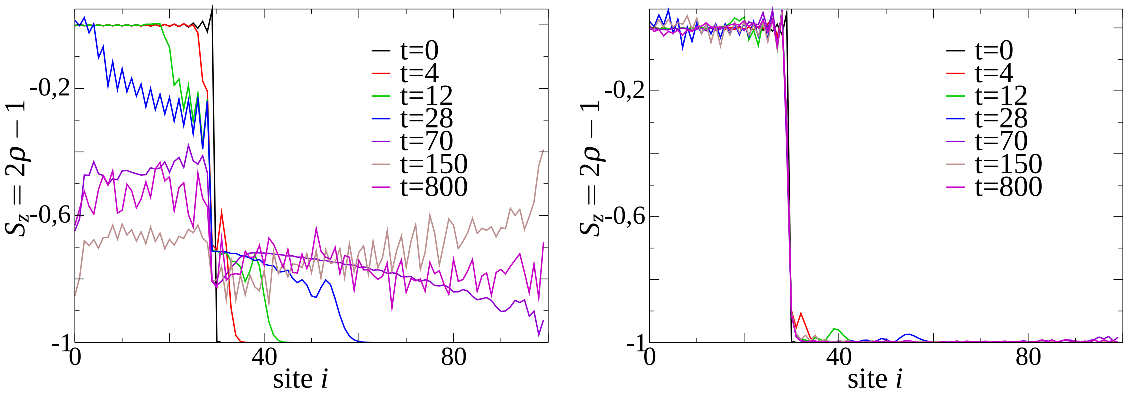

(c) $\mu_A = 1$ (d) $\mu_A = 2$

Figure 9: S_i^z at different points in time for different final potentials μ_A. $\mu_B = 0$. Initially we filled system A with $\mu_A = 0$, corresponding to half filling for $A = 30$, $L = 100$

7.5 Trapping

Interpreting the results of Figure 8 and Figure 9 in terms of bosonic particle occupation, we observe that for growing potential differences more and more particles are blocked inside the initial region.

This counterintuitive result is a consequence of energy conservation. The main difference with the classic system is, that we do not have an unbounded energy spectrum. For each site the allowed energy range is $\mu_i \pm 1$. Therefore a particle can only leave the high-potential region, if its loss in potential energy can be compensated by the gain of kinetic energy limited by ± 1 inside region B. The number of particles for which this is true decreases with the growing potential difference, because initially we filled states inside the whole kinetic energy range -1 to 1.

In the case $\mu_A - 1 \geq \mu_B + 1$ the minimum energy in A is always higher than the maximum energy in B and virtually all particles are blocked inside System A. We will call this phenomenon trapping. The small perturbations we still see are results of the tunnel effect, permitting the penetration of the System B modes into System A.

The results for an inverse potential $\mu_A \leq 0$ does not present any new information, if we just

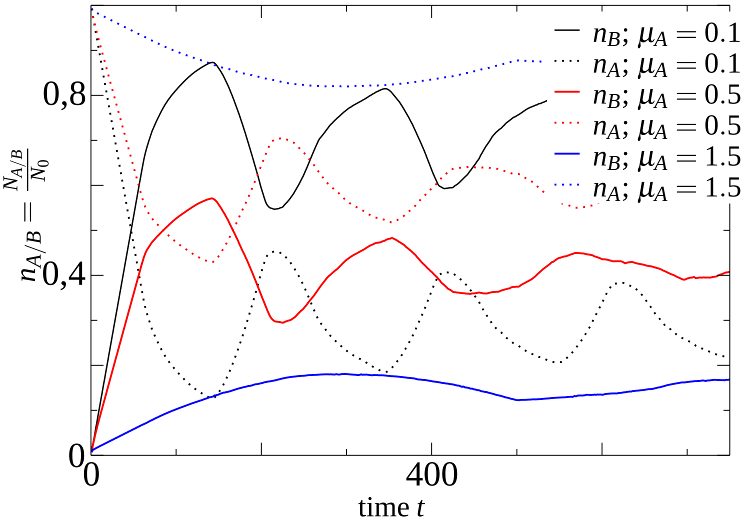

Figure 10: Percentage of particles in the left or right system as a function of time. Results for $A = 30, L = 100$, initially at zero temperature with complete filling for different final potentials and $\mu_B = 0$.

think of holes leaving from the right to the left following he same rules.

For the half filled initial state, only the low kinetic energy part of the initial system is filled and kinetic energies is conserved under the abrupt change of the potential, such that for the dynamics only the N modes of kinetic energy $-1\ldots0$ are significant, explaining the later inset of the trapping. This accounts also for the loss of symmetry of the perturbations running to the right and left, because the filling of the spectrum is not symmetric around zero kinetic energy.

7.6 Time-dependent Distribution of Particles in the left and right System

As we have seen before, the magnetization, which leaves the left region, is strongly influenced by the potential difference between the two systems. To clarify this behavior we change our point-of-view completely to considering bosonic particles. In Figure 10 we have plotted the percentage of particles in systems A and B as a function of time for different final values of μ_A. Before starting the evolution all N_0 particles were inside the left region, $\frac{N_A}{N_0} = 1$.

From what we have seen before, we expect the maximum of $\frac{N_B}{N_0}$ to be at $t^* = 2(L - A)$. At t^* particles that left System A at $t = 0$ and having been reflected at L start to reenter system A while slow moving particles had a maximum of time to escape from it. For high potential differences the fast propagating modes of system B at $\varepsilon_k \approx \mu_B$ with $v = c = 1$ are not occupied and we see a slower propagation.

The maximum of these curves can be seen as a measure for the number of particles which can actually reach System B. Our results underestimate the real number, because the system is finite and we measure the departed particle number at a finite time. In Figure 11 we show the behavior of $n_B = \frac{N_B(t)}{N_0}$ as a function of the system size. From the inset in Figure 11 we conclude that the committed error scales with $\frac{1}{L}$.

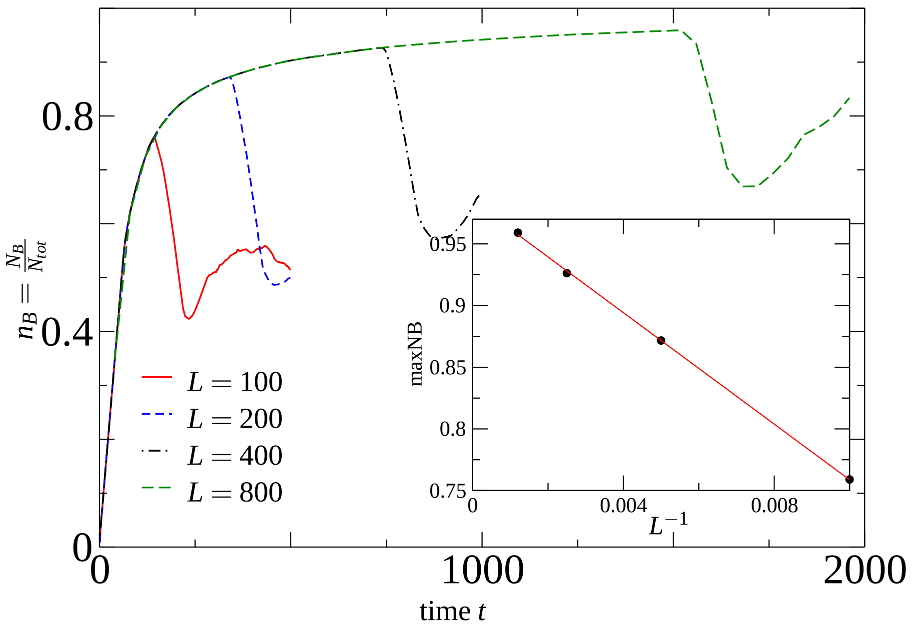

Figure 11: Percentage of particles in System B as function of time for different system sizes. Results for $A = 30$, $\mu_A - \mu_B = 0.75$, initially at zero temperature with complete filling ($N_0 = A$). The fit in the insert has the equation $n_{Bmax} = 0.98465 - 22.592\frac{1}{L}$

Let us suppose that the time t^* until the wave package going out to the right returns, does not suffice for slow particles to leave the initial region. We can make a quasi-classical development to get an approximative number of particles that have not yet left region A.

$$2A > v_q t^* \approx q_A^* 2(L-A) \Rightarrow N_{nondepart} \approx \frac{A}{\pi}\frac{A}{L-A} \sim \frac{1}{L}.$$

The dependence in A is more complicated due to quantized spectrum, which we have to take into account for small A.

Let us note as a summary, that we can optimize our results taking the parameters as follows:

A is to be taken small, but not so small as to introduce errors due to the quantization of one-particle modes in the left system. One can estimate that for most applications a value of $A > 20$ is necessary to eliminate those errors. L should be as big as possible, a number which is limited by the calculation time.

7.7 Time-Evolution of the kinetic and potential Energy

The whole dynamics is constrained by the conservation of energy (unitary dynamics). In Figure 12 we have represented kinetic and potential energy (as defined by (4.7)) for the initially completely filled and half filled system.

The graphs show the conservation of energy and the exchange between kinetic and potential energy due to the oscillations of the particle density between System A and B.

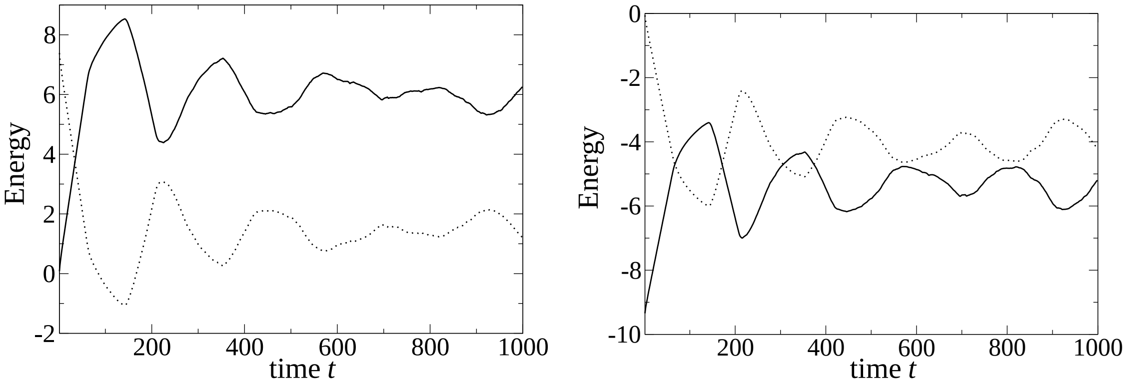

(a) completely filled System A, evolution for $\mu_A = 0.5$

(b) half filled System A evolution for $\mu_A = 0.5$

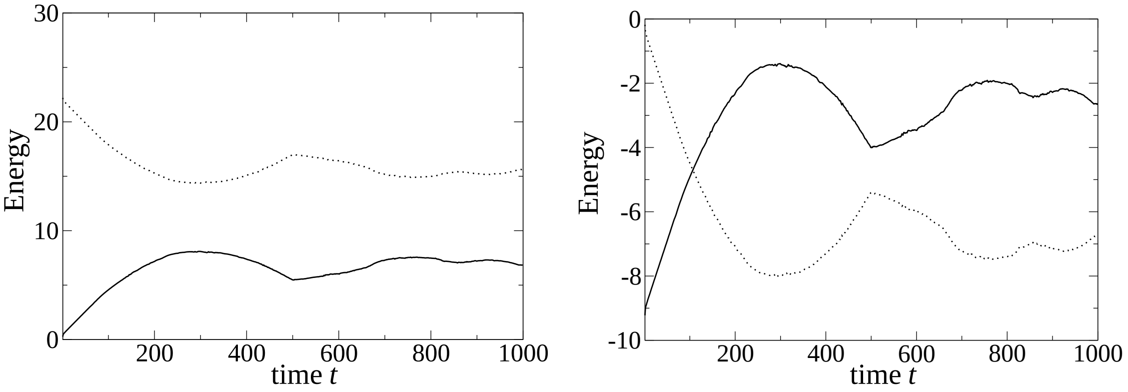

(c) completely filled System A, evolution for $\mu_A = 1.5$

(d) half filled System A, evolution for $\mu_A = 1.5$

Figure 12: Kinetic (solid line) and potential (dotted line) energy as a function of time for a system of $A = 30$ prepared zero temperature with $\omega = 1/2$ either half or completely filled. For the time-evolution we use $\mu_B = 0$.The free system $\mu_A = 0 = \mu_B$ has constant potential and kinetic energy, which would give straight lines.

We observe the important differences between the completely and half filled system behavior at $t \approx 0$. While for complete filling $E_{kin}(t = 0) = 0$ due to the symmetric kinetic energy spectrum, we have for half filling $E_{pot}(t = 0) = 0$ because $S_z = 0$ inside System A. For bosonic particles the data would have to be shifted by the constant value $E_0 = \frac{\mu_A A}{2}$.

7.8 Departure Dynamics

We have so far seen and understood the phenomenology qualitatively. Let us establish some quantitative results for the observed dynamics. First we have to know the initial state in terms of the new energy eigenfunctions.

7.8.1 Projection of the initial State onto the Energy Spectrum at $t > 0$

Let us define the initial one-particle eigenstates of the Hamiltonian at $t = 0$ as

$$\begin{array}{lll} \Psi_k^A(x) & k = 1 \dots A & \text{for states localized inside A} \\ \Psi_k^B(x) & k = A+1 \dots L & \text{for states localized inside B} \end{array}$$

Each state can be characterized by its wave number q_k^A or q_k^B respectively and vanishes in the other region.

The normalized one-particle eigenstates $\Phi_l(x)$ of the Hamiltonian at $t > 0$ are separated into the regions I,II and III (the different energy regions corresponding to permitted spacial regions A,A and B, B) given in Figure 4.

$$\begin{aligned} \Phi_l^I(x) =& \phi_l^A(x) && l = L - A' + 1 \dots L \\ \Phi_l^{II}(x) =& \alpha\, \phi_l^A(x) + \beta\, \phi_l^B(x) && l = B' \dots L - A' \\ \Phi_l^{III}(x) =& \phi_l^B(x) && l = 1 \dots B' \end{aligned}$$

where A' and B' depend on the potential difference and denote the number of states allowed only in System A or B resp. The functions ϕ_l^K are normalized, have a nonzero support only inside their respective region $K = A, B$ and are associated to the l-th overall energy level. Every ϕ_l^K level can be associated to a real wave number $q_l'^K$. The normalization of the states $\Phi_l^{II}(x)$ over the whole system yields

$$1 \overset{!}{=} \alpha^2 + \beta^2.$$

If furthermore we assume the amplitude of $\Phi_l^{II}(x)$ approximately equal inside A and B (the density has to be continous), this leads to $\alpha^2 \approx \frac{A}{L}$.

The initial Fock state created at $T = 0$ is

$$|\Psi_{total}\rangle = \prod_{k=1}^{N} \eta_k^+ |\emptyset\rangle$$

where $N \leq A$ is the total number of particles we create from the vacuum state $|\emptyset\rangle$.

Let us calculate the expectation value of the number of particles for a final state l, where $\mathbf{a}_l^+, \mathbf{a}_l$ are the creation and annihilation operators associated to the final energy eigenspectrum:

$$\begin{aligned} \langle \mathbf{n_l} \rangle &= \langle \Psi_{total} | \mathbf{a}_l^+ \mathbf{a}_l | \Psi_{total} \rangle \\ &= \langle \Psi_{total} | \sum_n \Phi_l(n) \mathbf{c}_n^+ \sum_m \Phi_l^*(m) \mathbf{c}_m | \Psi_{total} \rangle \\ &= \langle \Psi_{total} | \sum_{n,q} \Phi_l(n) \Psi_q(n) \eta_q^+ \sum_{m,k} \Phi_l(m)^* \Psi_k^*(n) \eta_k | \Psi_{total} \rangle \\ &= \sum_{k=1}^{N} \left| \sum_n \Phi_l(n) \Psi_k(n) \right|^2 \end{aligned} \tag{7.15}$$

We transform the spacial sum over n into an integral taking into account the different energy Regions I,II,III. This then yields (defining $\Delta = \mu_A - \mu_B$):

$$\begin{aligned} \langle n_l \rangle =& \sum_{k=1}^{N} \left(\sqcap(L-A' \ldots L; l)\, |I_{l,k}|^2 + \sqcap(B' \ldots L-A'; l)\, |\alpha\, I_{l,k}|^2 \right) && (7.16) \\ \text{with } |I_{l,k}|^2 =& \left| \sqrt{\frac{2}{A}} \sqrt{\frac{2}{A}} \int_0^A \mathrm{d}x \sin(q_l'^A x) \sin(q_k^A x) \right|^2 \approx \delta_{q'l,qk} \\ \Rightarrow f(q'^A) \approx& \Theta(q_N - q'^A) \left(\sqcap(\arccos(\Delta - 1 \ldots \pi, q'^A) + \frac{A}{L} \sqcap(0 \ldots \arccos(\Delta-1); q'^A) \right), \end{aligned}$$

where we have passed into the continuum case in wavenumbers by replacing the index dependency in l by the continous wavenumbers q'^A and n_l by the probability of occupation $f(q'^A)$. We can then use the density of states in the new system in terms of the wavenumbers q'^A (the wavenumber associated to states in system A at $t > 0$) $n(q'^A) = n_A(q'^A) + n_B(q'^A)$ as given by (7.5) to determine the particle density in the final system:

$$\begin{aligned} \rho(q'^A) \approx& (n_A(q'^A) + n_B(q'^A))\, f(q'^A) \\ =& \Theta(q_N - q'^A) \left(\sqcap(\arccos(\Delta-1) \ldots \pi; q'^A) \frac{A}{\pi} + \sqcap(0 \ldots \arccos(\Delta-1); q'^A) \frac{A+L-A}{\pi} \frac{A}{L} \right) \\ =& \Theta(q_N - q'^A) \sqcap(0 \ldots \pi; q'^A) \frac{A}{\pi} \\ =& \rho_0(q'^A) \end{aligned}$$

In this formula $\rho_0(q)$ denotes the density of particles inside an interval $\mathrm{d}q$ of the initial state.

So we can simply use the occupation density of the initial System A to calculate the density of particles in the new system.

For a given energy ω of the new system we can conclude for the occupation density in terms of energies using $\rho(\varepsilon)\,\mathrm{d}\varepsilon = \rho(q)\,\mathrm{d}q$ and $\rho(\omega)\,\mathrm{d}\omega = \rho(q_A')\,\mathrm{d}q_A'$

$$\rho(\omega) = \rho(\mu_A - \cos(q_A')) = \rho_0(\mu_A - \cos(q)) = \rho_0(\mu_A - \mu_0 + \varepsilon), \tag{7.17}$$

7.8.2 Modelisation of the Number of departing Particles in the Continuum Limit

Only the one particle energy eigenstates of $\mathbf{H}$ at $t > 0$ allowed inside System A and B can guarantee the transport of particles from one system into the other. We will call these modes, spanning the whole System, propagating modes. Inside A they are characterized by their wave number $q_A \in]0, \arccos(1 - (\mu_A - \mu_B))]$.

To calculate the number of particles leaving from system A, N_{esc}, is identical to calculating the initial density mapped onto the energy region $\mu_B - 1 < \omega < \mu_B + 1$ allowing for departure, where ω denotes the energy of the spectrum of $\mathbf{H}$ at $t > 0$. The initial density attributed to wavenumber q_0 is given by (c.f. 6.2)

$$\rho_0(q_0) = f(q_0) n(q_0) = \frac{A}{\pi} \sqcap(0 \ldots q_N; q_0) \quad \text{with} \quad q_N = \arccos(\mu_0).$$

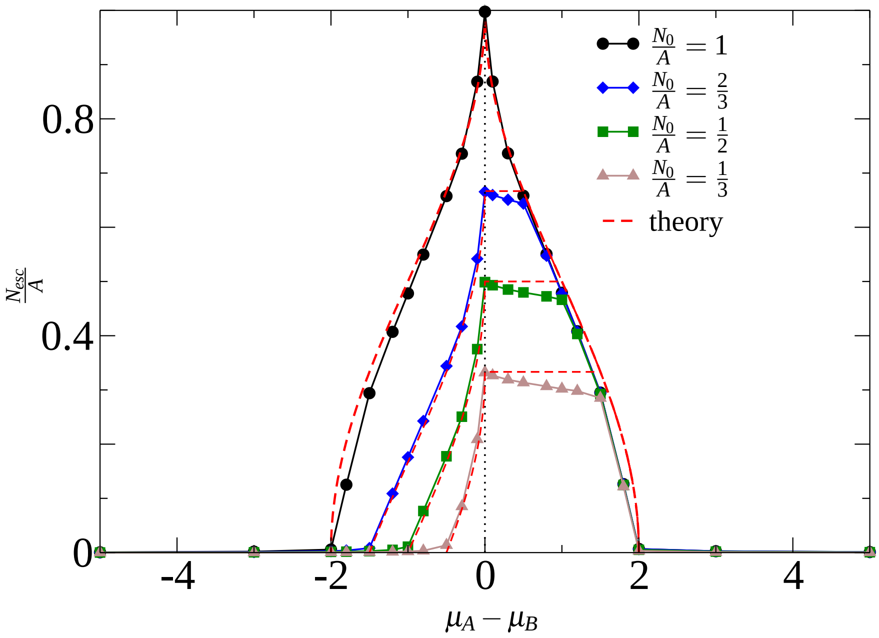

Figure 13: Particle density departing from the left zone as a function of the potential difference $\mu_A-\mu_B$. The different curves are made from different initial potentials $\mu_0=-8,-0.5,0,0.5$.

In the continuum limit $\frac{N_{esc}}{A}$ is then (for $\mu_A>\mu_B$) given by:

$$\begin{aligned}\frac{N_{esc}}{A}&=\frac{1}{A}\int_{\mu_B-1}^{\mu_B+1}\mathrm{d}\omega\,\rho(\omega)\\&=\frac{1}{A}\int_{q_A(\mu_B-1)}^{q_A(\mu_B+1)}\mathrm{d}q_A\,\rho(q_A)\\&=\frac{1}{A}\int_{0}^{\arccos(\mu_A-(\mu_B+1))}\mathrm{d}q_0\,\rho_0(q_0)\\&=\int_{0}^{\arccos(\mu_A-(\mu_B+1))}\mathrm{d}q_0\,\frac{\prod(0\ldots q_N,q_0)}{\pi}\end{aligned}\tag{7.18}$$

An analogous calculation can be done for $\mu_A<\mu_B$.

In Figure 13 we have represented the numerical and theoretical results for $\frac{N_{esc}}{A}$ for different initial filling heights. At $\mu_B-\mu_A=0$ the departure probability is 1 and we find the initial density $\frac{N_0}{A}$ inside region A. For great potential differences ($\mu_A-\mu_B>0$), the differently filled initial situations behave similarly, because only the filled part of the spectrum inside system A is in contact with system B ($q_N>\arccos(1-(\mu_A-\mu_B))$) in all cases.

The differnet situations for only propagating, only blocked states and a mixed situation is sketched in Figure 14.

If the potential difference is small enough to render non-filled states (at the top of the spectrum of System A) propagative, the number of escaping particles is limitied by the filling height and not by the forbidden energy of System B. This accounts for the cutoff positions of the graphs for

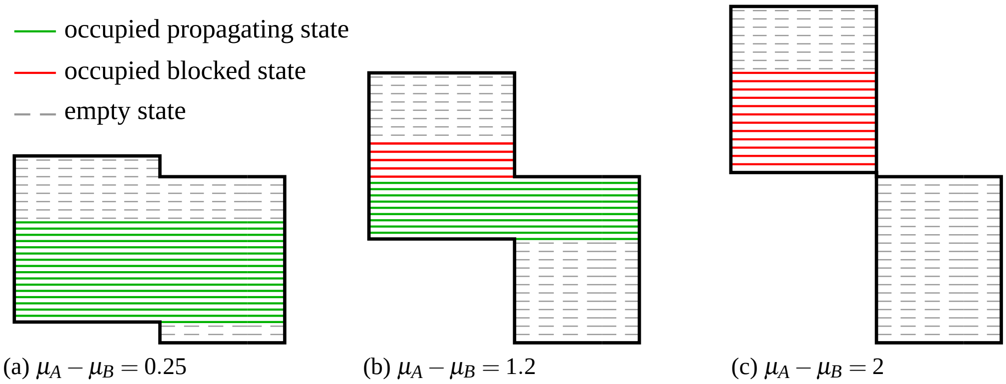

(a) $\mu_A - \mu_B = 0.25$ (b) $\mu_A - \mu_B = 1.2$ (c) $\mu_A - \mu_B = 2$

Figure 14: Energy spectrum for a given filling height with different final potential differences. Dashed lines symbolize non-occupied modes, solid states are occupied. Only particles in propagating modes (green) can escape to the right, while particles occupying modes localized in System A are blocked (red).

the region $\mu_A > \mu_B$ where all occupied states are in contact with a propagating mode. For $L \longrightarrow \infty$, the slope of this region tends to zero and is therefore a finite size effect.

The results and calculations for $\mu_A < \mu_B$ can be done and understood similarly. For small potential differences the first energy eigenstates rendered non-propagative are characterized by $\omega = \mu_A - 1$. But those are occupied such that we see a direct decrease of transported particles.

8 Dynamics of the Linear Potential

After having shown some basic properties in the rather simple case of a step potential, we now want to make a step towards a more general framework.

Starting with the same initial conditions as in the previous chapter we study the time-evolution induced by a linear potential for $t > 0$ (c.f. Figure 15).

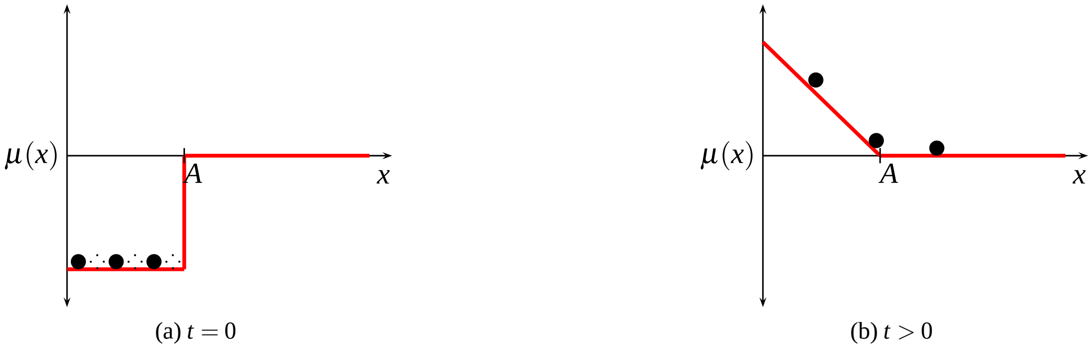

(a) $t = 0$ (b) $t > 0$

Figure 15: Schema of the experimental protocol in the case of a continous linear potential.

We consider

$$\mu_i = \begin{cases} \mu_B & \text{for} \quad A \leq i < L \\ \mu_A - \frac{\mu_A - \mu_B}{A} i & \text{for} \quad 0 \leq i < A \end{cases}.$$

As before we will call the left system ($0 \leq i < A$) "System A" and the right ($A \leq i < L$) "System B". For simplicity we mostly set $\mu_B = 0$.

Main differences to the previous chapter, that will have a significant influence are:

- The potential is continous at A, so we will not get energetically disconnected zones.
- No translation invariance inside System A along x
- Different potential structures for System A and B

We will first analyze the properties of the Hamiltonian and its spectrum for $t > 0$ before returning to analyze how the initial state looks in terms of this new spectrum and developing its dynamics.

8.1 Eigenstates and Energy Spectrum

The first step is again to diagonalize the Hamiltonian and identify the one-particle energy eigenmodes.

8.1.1 Eigenvectors

Writing the eigenvalue equation (3.11) results in

$$-\frac{1}{2}\Phi_k(i-1) + \mu_i \Phi_k(i) - \frac{1}{2}\Phi_k(i+1) = \varepsilon_k \Phi_k(i) \quad i = 0 \ldots L-1,\, k = 1 \ldots L \tag{8.1}$$

with ε_k the eigen-energy of the k-th eigenmode. We have set $\omega = \frac{1}{2}$ and $\mu_B = 0$.

We will again solve this equation separately for the subsystems A and B before introducing the quantification of states using the matching of the boundary conditions.

In System B we recover the same results as for the step potential:

$$\Phi_k(i) = \tilde{B}_k \sin(q_k i) \qquad \varepsilon_k = -\cos(q_k). \tag{8.2}$$

In System A, we transform (8.1) to a (continous) differential equation by considering the inter-site distance to tend to zero. This is possible by assuming slowly varying eigenfunctions $|\Phi_k(i) - \Phi_k(i-1)| \ll |\Phi_k(i) + \Phi_k(i-1)|$, which is only true for small $\varepsilon - \mu(x)$. It follows:

$$-\frac{1}{2}\frac{\mathrm{d}^2}{\mathrm{d}x^2}\Phi(x) = (\varepsilon - 1 - \mu_A)\Phi(x) + \frac{\mu_A}{A} x \Phi(x). \tag{8.3}$$

Now we transform to the new variable

$$\tilde{x} = -\left(\frac{2\mu_A}{A}\right)^{\frac{1}{3}} \left(x + \frac{A(\varepsilon + 1 - \mu_A)}{\mu_A}\right)$$

which yields, when put into (8.3):

$$\frac{\mathrm{d}^2}{\mathrm{d}\tilde{x}^2}\Phi(\tilde{x}) - \tilde{x}\Phi(\tilde{x}) = 0.$$

This is the differential equation defining Airy functions [1]. So we have the form of the solutions in this region as a linear combination $\Phi(x) = C_1\mathrm{Ai}(\tilde{x}) + C_2\mathrm{Bi}(\tilde{x})$ of two independent solutions of this equation.

The hypothesis of slowly varying functions needs a refinement. For a given energy, $\varepsilon - \mu(x)$ grows with x. Therefore we expect (in analogy with the step system) a high kinetic energy and short wavelengths when approaching the right boundary of System A. Furthermore we expect for System B all forbidden modes to be of unit wavelength. Therefore we put for the region $\varepsilon_k - \mu(x) > 0$

$$\tilde{\Phi}_k(i) = (-1)^i \Phi_k(i).$$

Using this ansatz inside (8.1) allows us the transformation to a differential equation of slowly varying $\tilde{\Phi}(x)$. Using the variables

$$\begin{aligned} \varepsilon_k' &= \mu_A - \varepsilon_k \\ x' &= A - x \end{aligned} \tag{8.4}$$

we recover (8.3).

So we can best describe a state by considering it separated into two spacial regimes. From the left $\varepsilon_k - \mu(x) \gtrapprox -1$, a state is described by $\Phi(x) = C_1\mathrm{Ai}(\tilde{x}) + C_2\mathrm{Bi}(\tilde{x})$. From the right ($\varepsilon - \mu(x) \lessapprox 1$) it is then given symmetrically by $\Phi(x) = (-1)^i C_1\mathrm{Ai}(\tilde{x}') + (-1)^i C_2\mathrm{Bi}(\tilde{x}')$, where we have to transform energy and position according to (8.4). In the middle between those two descriptions we expect a continous change from one to the other behavior. In the following we will mainly use the left solution and deduce the right by symmetry.

8.1.2 Energetically allowed Regions and Boundary Conditions at 0 and L

For System B at L we have the same boundary conditions as for the step potential, which have already been used implicitly to determine the solutions (8.2) given in the previous paragraph.

Expressing the Eigenfunctions for System A on the left in terms of the original variables we get:

$$\begin{aligned} \Phi(x) = \quad & C_1\mathrm{Ai}\left(-\left(\frac{2(\mu_A-\mu_B)}{A}\right)^{\frac{1}{3}}\left(x + \frac{A(\varepsilon+1-\mu_A)}{\mu_A-\mu_B}\right)\right) \\ & + C_2\mathrm{Bi}\left(-\left(\frac{2(\mu_A-\mu_B)}{A}\right)^{\frac{1}{3}}\left(x + \frac{A(\varepsilon+1-\mu_A)}{\mu_A-\mu_B}\right)\right). \end{aligned} \tag{8.5}$$

Analyzing the argument of these $\Phi(\tilde{x})$, we have for $\mu_B < \mu_A$ the following sign behavior:

$$\begin{aligned} \tilde{x} > 0 \quad \text{if} \quad x < A\frac{\mu(x) - 1 - \varepsilon}{\mu_A - \mu_B} \\ \tilde{x} < 0 \quad \text{if} \quad x > A\frac{\mu(x) - 1 - \varepsilon}{\mu_A - \mu_B} \end{aligned}$$

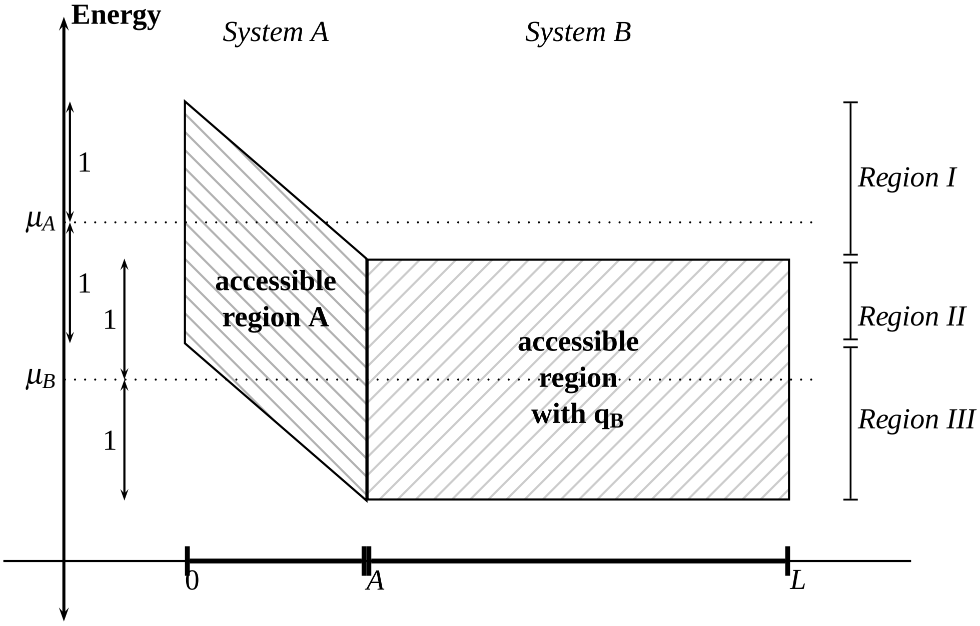

Figure 16: Schematic draft of the energetically accessible regions for the linear potential, where the accessible regions are limited by $\mu(x) \pm 1$ as shown in 8.1.2. We set $\omega = \frac{1}{2}$.

The sign change has a particular meaning in the argument of Airy functions. It marks the transition from oscillatory ($\mathrm{Ai}(\tilde{x} < 0)$ and $\mathrm{Bi}(\tilde{x} < 0)$) to decaying and diverging behavior (for $\mathrm{Ai}(\tilde{x} > 0)$ and $\mathrm{Bi}(x > 0)$ respectively). In terms of the energy, the sign change takes place at $\varepsilon = \mu(x) - 1$, marking the transition from an allowed (oscillatory) to a forbidden (decaying) energy region. Considering the solution to the right, the transition takes place at $\varepsilon = \mu(x) + 1$ as drafted in Figure 16.

In fact these considerations lead again to a separation into allowed ($|\varepsilon - \mu(x)| < 1$) and forbidden ($|\varepsilon - \mu(x)| > 1$) energy regions.

Let us divide the system into energy regions of different behavior as marked in Figure 16 to sum up their behavior at the boundaries and make conclusions about the prefactors C_1, C_2: The two regions to consider will be $\varepsilon < \mu_A - 1$ and $\varepsilon > \mu_A - 1$.

II, III $\mu_B - 1 < \varepsilon < \mu_A - 1$: The wave functions have to vanish for $x \leq 0 \Leftrightarrow \tilde{x} \geq 0$. So the rapidly diverging $\mathrm{Bi}(y > 0)$ function has a very small prefactor in comparison to the prefactor C_1 of $\mathrm{Ai}(\tilde{x} \gg 0) \approx 0$, namely $\frac{C_2}{C_1} \approx 0$. So for these regions we have approximately for all energies $\Phi(x) = C_1 \mathrm{Ai}(\tilde{x})$. This means that all states are equivalent on the diagonals parallel to $\varepsilon(x) = \mu(x)$ and therefore just shifted images of each other.

I $\mu_A + 1 > \varepsilon > \mu_A - 1$: $\mathrm{Ai}(\tilde{x}(x < 0)) = 0$ implies that the two contributions of the solution have to compensate each other at $x = 0$. The exact ratio $\frac{C_1}{C_2}$ can be calculated setting (8.5) to zero at $x = 0$. This result however is not of obvious use due to the complex structure of the Airy functions and we will thus leave it at this rather structural formulation.

For the functions describing the behavior near the right boundary, we of course obtain the same behavior superposed by the oscillations of unit wavelength.

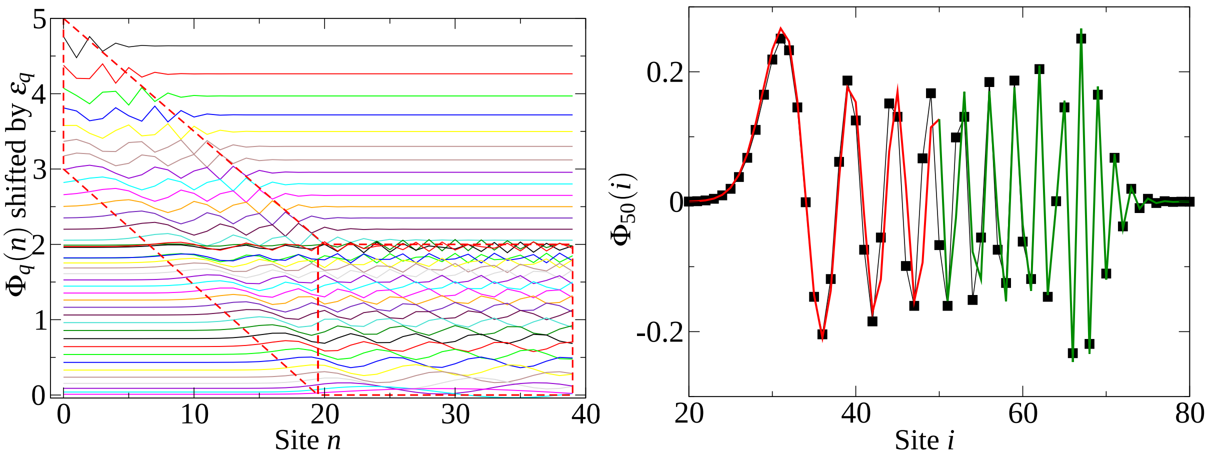

(a) (b)

Figure 17: Left: $\Phi_q(n)$ shifted by their associated energy eigenvalues for a system of $L = 40$ sites using $\mu_A = 3$, $\mu_B = 1$, $\omega = 0.5$, $A = 20$. The dashed line represents the boundaries of the allowed energy regions. Right: $\Phi_{50}(n)$ numerical data (squares) and approximation on the left and right by the Airy function solutions $\Phi(i) = \Phi(A-i)(-1)^i, i = 0 \ldots A/2$. $L = 100$ sites using $\mu_A = 5$, $\mu_B = 0$ in a purely linear system.

8.1.3 Boundary Conditions at A

In principle, we will observe a quantification of the allowed energy values ε_k due to the matching conditions of the eigenfunctions at the interface between Systems A and B. Calculating the exact states, however, is a nontrivial task. Furthermore we will need for our further development only approximations such that the exact matching conditions are not of immediate necessity for this work.

To complete the picture let us consider the region above the allowed energies $\varepsilon_k > \mu(x) + 1$. As for the step potential above the allowed energy region for $x > A$, we observe for $\Phi_k(x)$ a (Airy-Function) decay with a sign change at every site inside the forbidden energy region.

In Figure 17a, the results of our numerical diagonalization for the states are shown shifted by their eigenenergies. We can distinguish the two regimes of oscillations with diminishing wavelength in System A and sinusoidal behavior in System B. Furthermore we observe the rapid decrease outside the allowed regions. Notice the invariance of the states of energy ε inside p$\mu_B + 1 < \varepsilon < \mu_A - 1$ when shifted in parallel with the potential inside System A.

A comparison of the numerically obtained states with the Airy function solutions yields a good agreement (c.f. Figure 17b). There is however a difference in the behavior near $x = \frac{A}{2}$ due to the fact that the hypothesis $\frac{\mathrm{d}\,\Phi_q(i)}{\mathrm{d}i} \ll 1$ resp. $\frac{\mathrm{d}\,(-1)^i\Phi_q(i)}{\mathrm{d}i} \ll 1$ are no longer invalid.

8.2 Density of States

For later use inside integrals in a quasi-continous energy band approximation we calculate the density of states $n(\varepsilon)$. Let us recall that every energy state has one root more than its predecessor

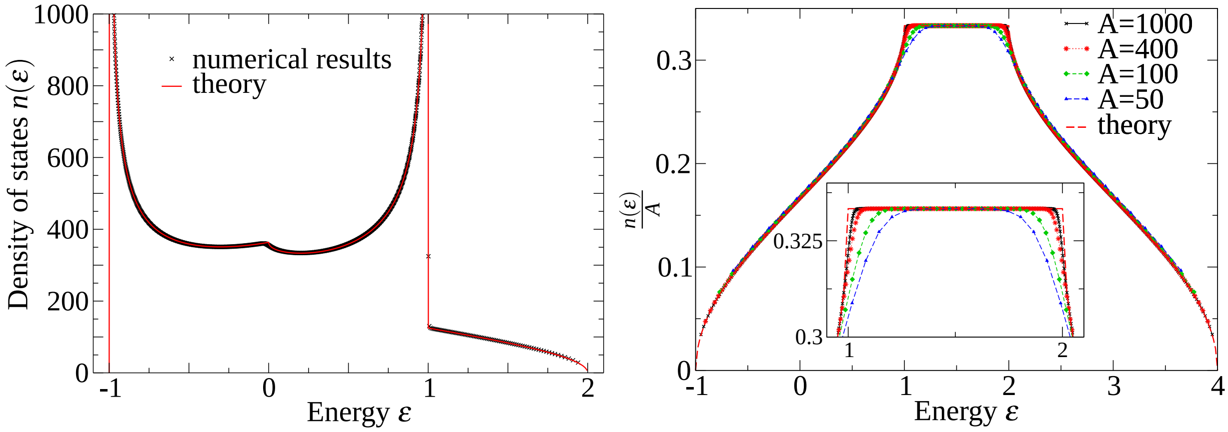

(a) $\mu_A = 1, \mu_B = 0, L = 1000, A = 250$

(b) $A = L, \mu_i = \mu_A - \mu_A \frac{i}{A} \quad \mu_A = 3$

Figure 18: Left: Comparison of the numerical and theoretical results for the density of states for the linear potential. Right: Purely linear system density of states for different system sizes.The flat zone in the middle disappears for $\mu_A < 2$

in energy and the additivity of the densities of two spacial subsystems (see Figure 7.2).

We separate System A and B and calculate their respective densities of states: For system B the result is identical to the one found for the step potential (see (7.5))

$$n(\varepsilon)_B = \frac{n(q_B)}{\sqrt{1-(\varepsilon-\mu_B)^2}}.$$

For system A a similar approach is successful. Let us treat System A as if it consisted of a series of infinitesimal subsystems of size dx which each has locally the same properties as a flat potential. We can then consider every single of these subsystems to be locally at equilibrium. Inside each interval $x \ldots x + \mathrm{d}x$ we define the local $n(\varepsilon, x)$.

By integrating over the contributions to the density of states along x we determine the density of states for a given value of the energy. The reasoning why this should work is, that the difference in energy $\frac{1}{n(\varepsilon)} = \varepsilon_{k+1} - \varepsilon_k$ only depends on the zeros of the states $\Phi_k(x), \Phi_{k+1}$ and not on their amplitude. So the unknown amplitude (a function of x) is of no importance and we only have to know the (local) wavelength (resp. the wavenumber) at x, which directly depends only on $\varepsilon - \mu(x) = -\cos(q_k)$ for every interval dx. In analogy with the results in the step potential (7.5) we define the local density of states as

$$n(\varepsilon, x) = \frac{\sqcap\!\sqcap(\mu(x) - 1 \ldots \mu(x) + 1; \varepsilon)}{\pi\sqrt{1-(\varepsilon-\mu(x))^2}},$$

where the spatial dependency is solely carried by the explicitly x-dependent chemical potential and $\sqcap\!\sqcap(a \ldots b; x)$ represents the door function (c.f. (4.1) in 4.1 for the formal definition).

Let us carry out the integration over x, while keeping track of the boundary values when changing the variable to $y = \varepsilon - \mu(x) = \varepsilon - \mu_A + \frac{\mu_A - \mu_B}{A} x \quad \in [-1, 1]$:

$$\begin{aligned} n(\varepsilon) &= \int_0^A \mathrm{d}x \, n(\varepsilon, x) \\ &= \int_{-1}^{1} \mathrm{d}y \, \frac{A}{\mu_A - \mu_B} \frac{\sqcap(0 \ldots A; x)}{\pi\sqrt{1-y^2}} \\ &= \frac{A}{(\mu_A - \mu_B)\pi} \arccos(y) \Bigg|_{y=\alpha}^{y=\beta} \end{aligned} \tag{8.7}$$

where for a given energy, α is the minimum over allowed x of $\varepsilon - \mu_A(x)$, while β is its maximum. Let us solve this by considering the boundaries of the allowed energy regions separately. For each of them we plug their extremal allowed values α or β into (8.7). Treating the boundaries one by one, we get:

- Right boundary ($x = A$): Energy range $\mu_B - 1 < \varepsilon < \mu_B + 1$ gives $\beta = \varepsilon - \mu_B$.
- Right/Top boundary: $x = \mu_A + 1 - \frac{A}{\mu_B - \mu_A}\varepsilon$: Energy range $\mu_B + 1 < \varepsilon < \mu_A + 1$ gives $\beta = 1$.
- Left boundary: ($x = 0$): Energy range $\mu_A - 1 < \varepsilon < \mu_A + 1$ gives $\alpha = \varepsilon - \mu_A$.
- Left/Bottom boundary ($x = \mu_A - 1 - \frac{A}{\mu_B - \mu_A}\varepsilon$): Energy range $\mu_B - 1 < \varepsilon < \mu_B + 1$ gives $\alpha = -1$.

To cast the result in a readable form while taking into account the different overlapping regions it is most convenient to write the result in terms of the door function to always chose the appropriate interval.

The total density of states for all those regions and including the results for $\mu_B > \mu_A$, for which an analogous calculation can be done, then reads

$$n(\varepsilon) =$$

$$+ \quad \sqcap(\mu_B - 1 \ldots \mu_B + 1; \varepsilon) \frac{L - A}{\pi} \left(1 - (\mu_B - \varepsilon)^2\right)^{-\frac{1}{2}} \tag{8.8a}$$

$$+ \quad \sqcap(\mu_B - 1 \ldots \mu_B + 1; \varepsilon) \frac{A}{\pi(\mu_A - \mu_B)} \arccos(\mu_B - \varepsilon) \tag{8.8b}$$

$$+ \quad \sqcap(\mu_B + 1 \ldots \mu_A + 1; \varepsilon) \frac{A}{\mu_A - \mu_B} \tag{8.8c}$$

$$+ \quad \sqcap(\mu_A + 1 \ldots \mu_B - 1; \varepsilon) \frac{A}{\mu_B - \mu_A} \tag{8.8d}$$

$$- \quad \sqcap(\mu_A - 1 \ldots \mu_A + 1; \varepsilon) \frac{A}{\pi(\mu_A - \mu_B)} (\arccos(\mu_A - \varepsilon)). \tag{8.8e}$$

In this formula, (8.8a) reflects the contribution from system B while the other contributions are those of the boundaries of system A. (8.8c) and (8.8d) give the contribution of the upper diagonal boundary for the case of a positively or negatively tilted potential.

In Figure 18a we compare the resulting function with the numerical data.

Before we use these results to evaluate dynamical properties, let us evaluate if the size of the system has a significant influence. For the continous limit we basically placed ourselves in an infinite system, so we expect the calculated results to be the limit of the numerical curves when $L \to \infty$.

In Figure 18b we show the curves obtained numerically and analytically for different system sizes. We have separated the linear System A from the flat System B to eliminate the superposition of their states and give a clearer picture. The errors, we find are small even for small systems. So the use of this approximation will not introduce great errors due to finite size.

In fact the technique used here can be generalized to work with many other forms of potentials. As this leaves the main focus of this work, this result can be found in the Appendix A.

8.3 Time-Evolution of the Density Profile

In this section we will show the numerical results for the evolution of the initial state placed inside a linear potential and then try to understand some of the dynamical phenomena we observe. After an analysis of the departure dynamics the main focus will be on the trapping region. We will mostly treat the case of a repulsive potential $\mu_A > \mu_B$.

In Figure 19 the numerical results for the dynamics in the linear case for different initial states and slopes of the final potential are shown. As for the step potential case we see that part of the particles leave to System B, forming a wave package. Inside the initial region we have a more and more pronounced trapping effect for increasing potential differences.

8.4 Departure Dynamics

8.4.1 Projection of the Initial State onto the new System

In the same way as in the step potential case we investigate the number of particles initially localized in System A leaving to System B. A formal projection of the initial states onto the final system is however an arduous task.

We can nevertheless understand some basic properties of the projection by recurring to the classical picture of infinitesimal droplets with well defined momentum and position corresponding quantum-mechanically to a coarse-graining in q. We consider a density of infinitesimal droplets of mass $\rho_q(x)\,\mathrm{d}x\,\mathrm{d}q$, which is equivalent to

$$\rho_q(x)\,\mathrm{d}q\,\mathrm{d}x = \frac{\sum\limits_{\tilde{q}=q-\frac{m}{2}}^{q+\frac{m}{2}} \left|\Phi_{\tilde{q}}(x)\right|^2 \mathrm{d}x}{m}\,\mathrm{d}q \quad \text{with} \quad L \gg m$$

The initial density is created by the superposition of the N lowest energy eigenstates (characterized by $q < q_N$) $\Phi_q(x) = \tilde{A}\sin(qx)$ with an occupation

$$f(q) = \sqcap(0\ldots q_N; q)$$

with $q_N = \arccos(\mu_0)$, where we use $\mu_0 = \mu_A(t=0)$. We assume that in the continuum limit the

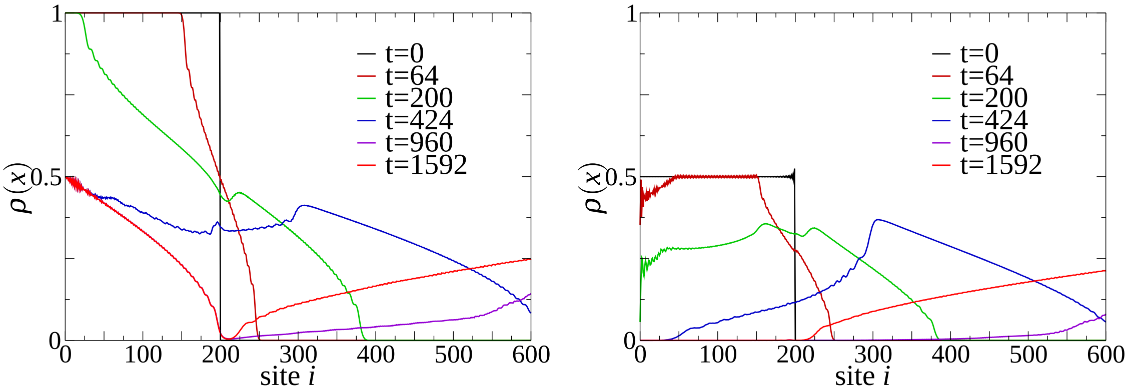

(a) completely filled, $\mu_A = 1$

(b) half filled, $\mu_A = 1$

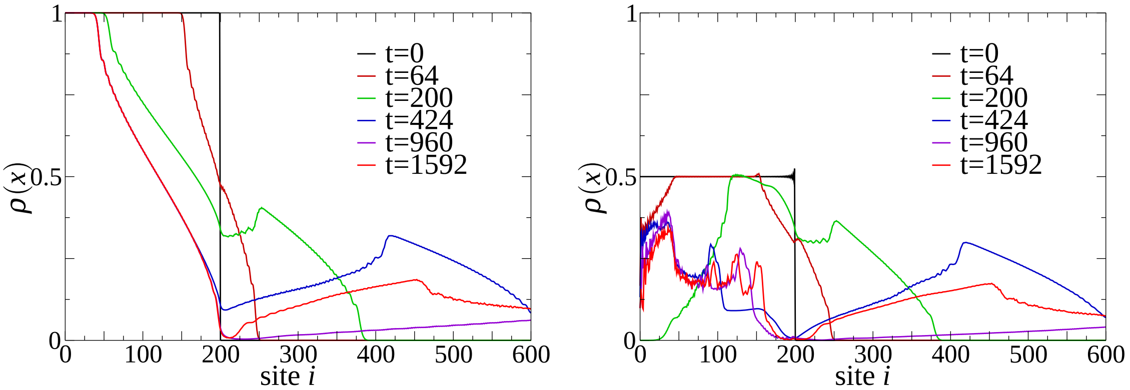

(c) completely filled, $\mu_A = 2,5$

(d) half filled, $\mu_A = 2,5$

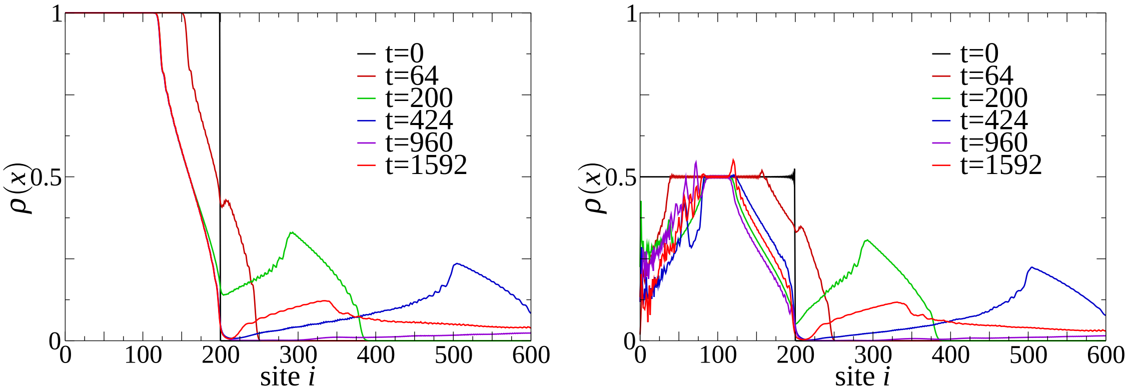

(e) completely filled, $\mu_A = 5$

(f) half filled, $\mu_A = 5$

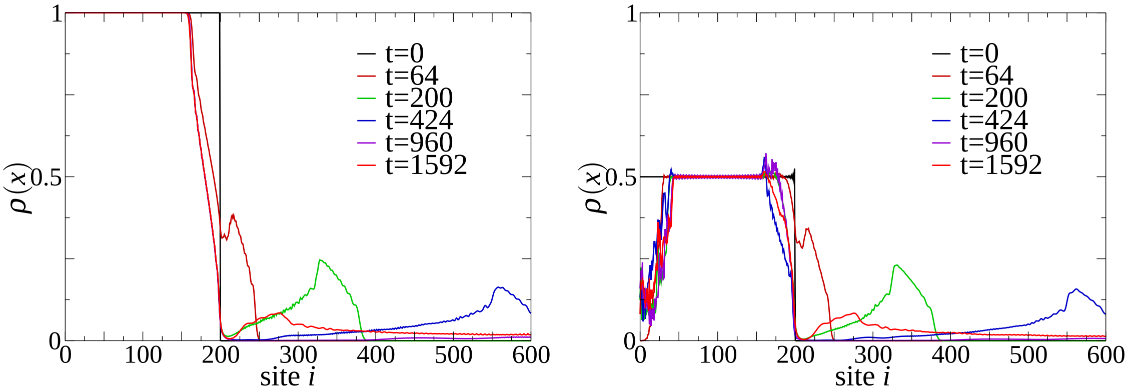

(g) completely filled, $\mu_A = 10$

(h) half filled, $\mu_A = 10$

Figure 19: Density of particles on a chain of $L = 1000, A = 200, \mu_B = 0$ for different initial fillings and slopes of the potential at $t > 0$.

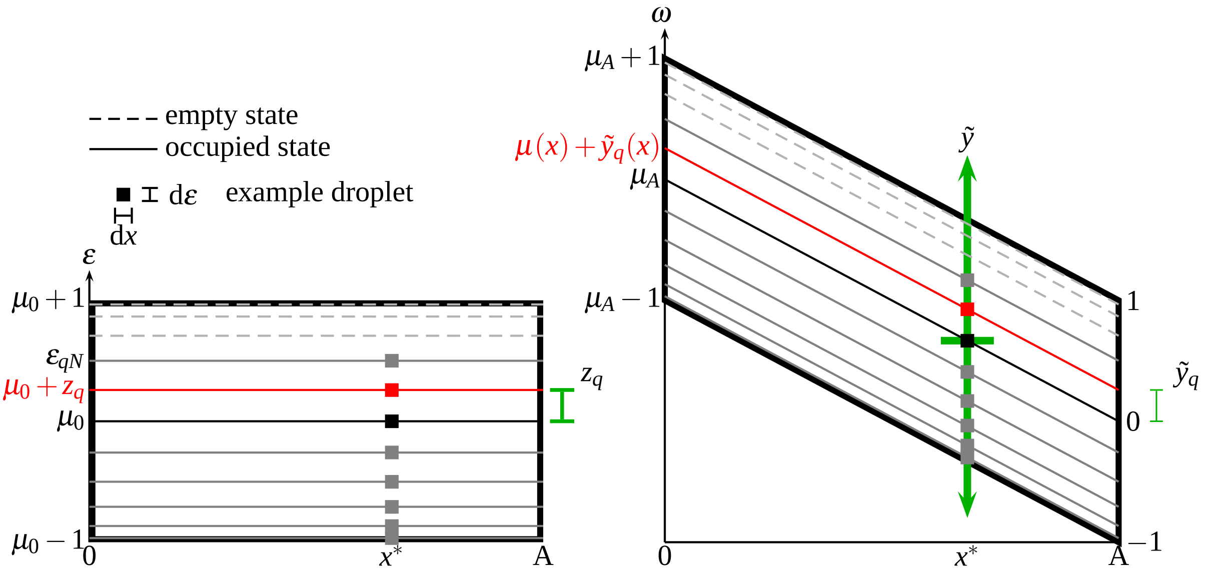

(a) t=0 (b) t=0+

Figure 20: Initial and final positions of infinitesimal droplets at position x^* inside the initial and final system. The lines represent the initial eigenstates of the Hamiltonian. The example droplets preserve their position in x and the kinetic energy $z_q = y_q$ (the distance from μ_0 resp. $\mu_t(x)$)

coarse-grained particle density is approximately uniform for means over small volumes $\Delta q\Delta x$:

$$\frac{\int_x^{x+\Delta x}\sum_{k=m}^{m+\Delta q}|\Phi_m(x)|^2\,\mathrm{d}x}{\Delta q\Delta x}\approx Const.=1.$$

We obtain then for the density in x and q

$$\rho_q(x)\,\mathrm{d}x\,\mathrm{d}q\approx\frac{\mathrm{d}x}{A}f(q)n(q)\,\mathrm{d}q,$$

where $n(q)$ is the local density of states as defined in 8.2. Therefore, the initial density associated to the wavenumber q at a given position is independent of x and given by

$$\rho_q^0(x)=\frac{1}{A}n(q)f(q)=\frac{1}{\pi}\sqcap(0\ldots q_N;q).$$

We use (the kinetic energy of q)

$$z_q=\varepsilon_q-\mu_0=-\cos(q)<-\cos(q_N).$$

Let us determine the projection of the density. While quenching, every single droplet is mapped into the new system in a way that conserves its position x and kinetic energy z_q.

The energy inside the new system is denoted by ω and the potential by $\mu_t(x)$. The condition for the conservation of kinetic energy yields for any x (introducing the new variable $\tilde{y}=\omega-\mu_t(x)$ as the kinetic energy in the new system):

$$\tilde{y}_q=\omega-\mu(x)\overset{!}{=}\varepsilon_q-\mu_0=z_q=-\cos(q). \tag{8.9}$$

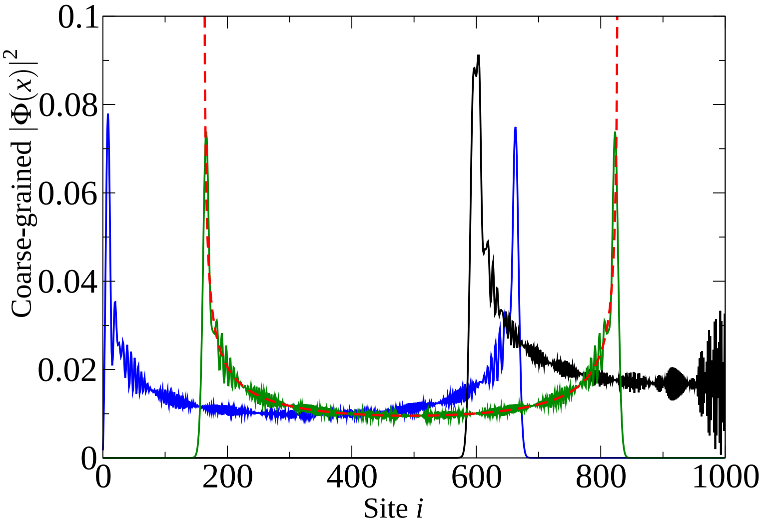

Figure 21: Results for $\rho_k(x) = \frac{1}{10}\sum_{\tilde{k}=k}^{k+9}|\Phi_{\tilde{k}}(x)|^2$ with (from left to right) $\tilde{k} = 661\ldots670$, $\tilde{k} = 491\ldots500$ and $\tilde{k} = 131\ldots140$. The dashed line represents the profile calculated using (8.12)

The initial density associated to a given value of z_q is therefore projected onto a line parallel to $\mu(x)$ given by $\omega = \tilde{y}_q + \mu(x)$ with $\tilde{y}_q = z_q$.

A sketch of this mapping of droplets is given in Figure 20.

The density is conserved throughout the mapping and we get using (8.9) :

$$\rho(\tilde{y},x)\,\mathrm{d}\tilde{y}\,\mathrm{d}x = \rho_q^0(x)|_{\tilde{y}=-\cos(q)}\,\mathrm{d}q\,\mathrm{d}x \tag{8.10}$$

The final density only depends on x through the value of $\tilde{y}(x^*)$ and we omit the variable x:

$$\rho(\tilde{y})\,\mathrm{d}\tilde{y}\,\mathrm{d}x = \rho_q^0(x)\,\mathrm{d}q\,\mathrm{d}x = \frac{1}{\pi}\mathrm{d}q\,\mathrm{d}x, \tilde{y} = -\cos(q) \tag{8.11}$$

So we get

$$\rho(\tilde{y}) = \frac{1}{\pi}\frac{1}{\sqrt{1-\tilde{y}^2}}\sqcap(-1\ldots-\cos(q_N),\tilde{y}).$$

Explicitly using $\tilde{y}(x)$ we can represent the density as a function of x for a given energy ε using $\tilde{y} = \varepsilon - \mu_A(1-\frac{x}{A})$:

$$\rho(x) = \frac{1}{\pi}\frac{\mu_A}{A\sqrt{1-(\varepsilon-\mu_A(1-\frac{x}{A}))^2}}\sqcap(\frac{A}{\mu_A}(\mu_A-\varepsilon+1)\ldots\frac{A}{\mu_A}(\mu_A-\varepsilon+\cos(q_N)),x) \tag{8.12}$$

We expect a density profile of this form inside the linear region in the coarse-grained model. This is well reproduced numerically as can be seen in Figure 21.

8.4.2 Modelisation of the Number of departing Particles in the Continuum Limit

To calculate the number of particles, that will leave the system A, N_{esc}, we have to count the number of particles mapped into the energy region $-1\ldots+1$, setting $\mu_B = 0$. Those particles

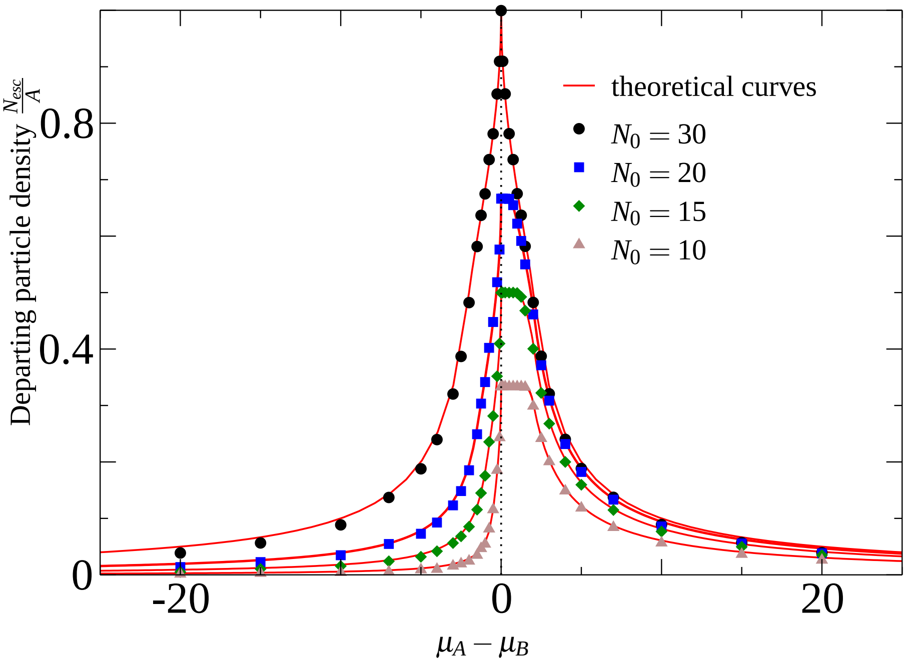

Figure 22: Particle density departing from the left zone as a function of the potential difference ($\mu_B = 0$). The different curves represent simulations for different initial filling densities. We used $L = 2000, A = 30$.

will be occupying propagative modes and therefore leave to System B. This is equivalent to $\tilde{y} = -\cos(q) \in [-1, 1 - \mu_A(1 - \frac{x}{A})]$ if $\mu_A > 0$.

N_{esc} is therefore given by the following integral (for $\mu_A > 0$):

$$\begin{aligned}
\frac{N_{esc}}{A} &= \frac{1}{A}\int_0^A \mathrm{d}x \int_{-1}^{1} \mathrm{d}\omega\, \rho(\tilde{y}(\omega, x)) \\
&= \frac{1}{A}\int_0^A \mathrm{d}x \int_0^{\pi} \mathrm{d}q\, \rho^0(q) \sqcap (0 \ldots \arccos(\mu_A(1 - \frac{x}{A}) - 1), q) \\
&= \frac{1}{A\pi}\int_0^A \mathrm{d}x \int_0^{\arccos(\mu_A(1-\frac{x}{A})-1)} \mathrm{d}q\, \Theta(\arccos(\mu_0) - q))\Theta\left(x - A(1 - \frac{2}{\mu_A})\right) \\
&= \frac{1}{A\pi}\int_0^A \mathrm{d}x \arccos(\mu_A(1 - \frac{x}{A}) - 1)\Theta(\arccos(\mu_0) - q))\Theta\left(x - A(1 - \frac{2}{\mu_A})\right) \qquad (8.13)
\end{aligned}$$

This integral has to be evaluated separately for different values of μ_A. Calculating in the same way also the case of $\mu_A < 0$, the final result reads

$$\frac{N_{esc}}{A} = \frac{1}{\pi\,|\mu_A|}\begin{cases} \sqrt{1-\mu_0^2}+\arccos(\mu_0) & \text{for} \quad 2 < \mu_A \\ \left[\begin{array}{c} (\mu_A-1)\arccos(\mu_A-1)+\arccos(\mu_0) \\ +\sqrt{1-\mu_0^2}-\sqrt{\mu_A(2-\mu_A)} \end{array}\right] & \text{for} \quad 1+\mu_0 < \mu_A < 2 \\ \arccos(\mu_0) & \text{for} \quad 0 < \mu_A < 1+\mu_0 \cdot \\ \left[\begin{array}{c} (\mu_A+1)\arccos(\mu_A+1)-\mu_A\arccos(\mu_0) \\ -\sqrt{-\mu_A(2+\mu_A)^2} \end{array}\right] & \text{for} \quad \mu_0-1 < \mu_A < 0 \\ -\sqrt{1-\mu_0^2}+\arccos(\mu_0) & \text{for} \quad \mu_A < \mu_0-1 \end{cases}$$

The numerical results for $\frac{N_{esc}}{A}$ and theoretical curves are shown in Figure 22. We see a good agreement for the result as long as Δ is small. For large $|\mu_A|$ the coarse-graining hypothesis does no longer hold true inside the integration region.

The employed technique can also be applied to calculate the number of particles mapped into any other given energy range. The main result to retain is that the number of escaping particles is proportional to the inverse of the slope of the potential $N_{esc} \propto \frac{A}{\Delta}$.

8.4.3 Potential-independent Features

For our given partially filled initial state, which is quenched to any new potential, we always observe two different regimes for the departure probability. First, if all occupied modes of the energy eigensystem at $t > 0$ are propagative and second if we have modes blocked by the potential difference. We can actually determine the coordinates of this transition for any potential with $\frac{\mathrm{d}\,\mu(x)}{\mathrm{d}x} > 0$, by considering the conservation of kinetic energy (and therefore $\varepsilon - \mu(x) = cos(q_N)$ over the quench. By taking

$$\mu_B + 1 = \mu_A - \mu_0 = \mu_A - \cos\left(\frac{\pi N_0}{A}\right)$$

to get the potential difference Δ rendering the highest energy states non-propagative, we get the coordinates at the point of transition

$$(\Delta, \frac{N_{dep}}{A}) = \left(1+\cos(\frac{\pi N_0}{A}), \frac{N_0}{A}\right), \tag{8.14}$$

where $\frac{N_0}{A}$ corresponds to the initial filling ρ^0. These results correspond well to the graphs we have shown so far for the linear and the step potential (c.f. Figures 13,22).

8.5 Characterization of the Blocked Particles

Let us return to the linear potential dynamics.The package of departing particles is just a propagating density on a flat potential. It is therefore of minor interest and has already been extensively studied (e.g. [11]). We can always choose L big enough to see it dispersing. However inside the region of the linear potential we observe a persisting dynamics of the trapped particles. In Figure

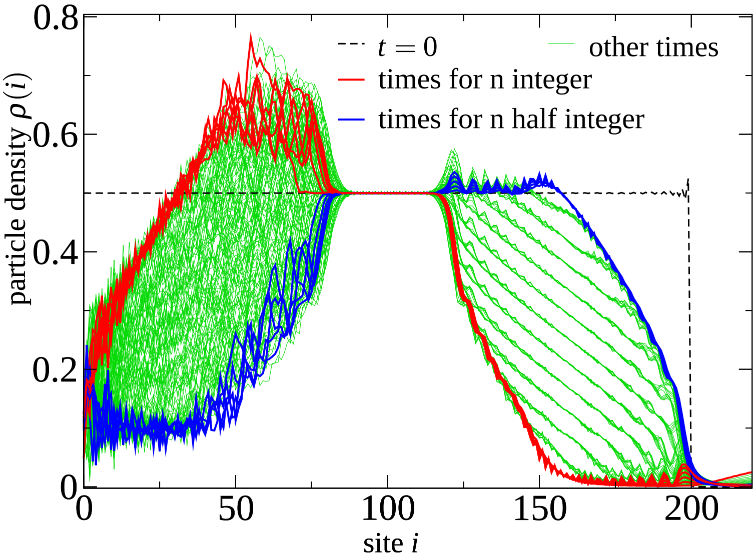

Figure 23: Zoom on the linear potential region $0 \ldots A$ for $\mu_A - \mu_B = 5$, $L = 1000, A = 200$. The curves represent different times $t = 2\pi \frac{A}{\mu_A - \mu_B} \frac{n}{24}$ $n = 0, 12, 13, \ldots, 149, 150$. States corresponding to $\frac{n}{24}$ integer and half integer have been marked especially. The reason for this choice of times will be obvious after the following discussions

23 we have superposed numerical results for the densities of particles at many points in time which allows us to explicitly see some of the main features and dynamical properties, we will quantify in the following.

To better understand the dynamics, let us recall the system's energy ranges and analyze their behavior separately.

- $\mu_B - 1 < \varepsilon < \mu_B + 1$: Particles in this energy region will leave to system B, because they occupy propagative modes.
- $\mu_B + 1 < \varepsilon < \mu_A - 1$: Every energy eigenstate can be constructed from any other Eigenstate by just shifting it in parallel with the potential. Density of states is $n(\varepsilon) = \frac{A}{\mu_A - \mu_B}$. Particles occupying these states are trapped.
- $\mu_A - 1 < \varepsilon < \mu_A + 1$: Particles occupying states in this energy range are trapped as well. The Eigenstates are superpositions of $\mathrm{Ai}(\tilde{x})$ and $\mathrm{Bi}(\tilde{x})$ and therefore hard to calculate exactly.

The three regions are drafted in the Figure 24a.

8.6 Plateau

The most striking feature in Figure 23 is the formation of a flat region in the middle of the linear potential region. A closer look at the allowed energy regions and the energy spectrum gives a

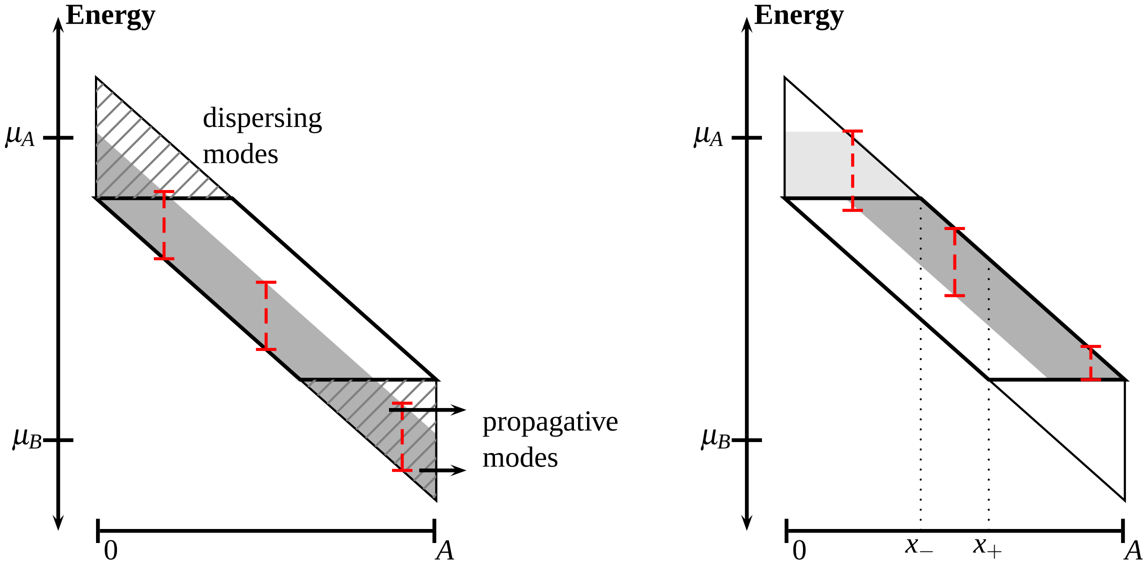

(a) $t = 0$ (b) $t = \frac{2\pi A}{\mu_A - \mu_B}(n + \frac{1}{2}), n \gg 1$

Figure 24: Schematic draft of the energetically accessible regions for the linear potential. Density in the upper (hatched) part ($\mu_A - 1 < \varepsilon < \mu_A + 1$) is dispersing over time, the lowest modes (hatched) with $-1 < \varepsilon < 1$ are the propagative modes. The remaining modes (inside the bold black parallelogram) are equidistributed and homogeneous and therefore exhibit identical transportation properties on parallels to $\mu(x)$. The gray surface shows the spacial distribution of the density of particles. The observed density at a given position x is obtained by superposing the density of all allowed energies. The dashed lines represent the integration range over the homogeneous modes to obtain $\rho(x)$ at three example positions of x. Inside $x_- < x < x_+$ content of the integration range stays identical over time.

hint to its explanation. In fact the plateau occupies exactly the spatial range, where only states inside the energy region $\mu_B + 1 \ldots \mu_A - 1$ are allowed (c.f. the region not hatched in Figure 24a).

As a consequence of the spacial invariance of the initially created state and the states in this energy region, all the allowed states inside this region are uniformly filled at $t = 0$. They are independent, evolve identically under time-evolution but are slightly shifted in x against each other. As before, their filling and behavior does only depend on the value of $\tilde{y} = \omega - \mu(x)$ and not on energy and position directly. Therefore all density on a line in parallel to $\mu(x)$ is identical in value and moves with the same velocity. If, to fix the ideas, at a given position x density is leaving to the right for a given energy ε there is always the same density taking its place from the left introduced by a state of $\varepsilon + \mathrm{d}\varepsilon$, if the state $\varepsilon + \mathrm{d}\varepsilon$ belongs to $\mu_B + 1 \ldots \mu_A - 1$. We therefore basically observe a displacement of a block of constant density along x for the density associated to a given initial value of $\tilde{y}$. This is illustrated by Figure 24, where two points in time are shown.

Therefore any density at position x resulting from the superposition of only states showing this behavior stays unchanged over time. The initial shape of the particle density, which is the flat plateau is then preserved. In Figure 24b we mark the border of the region in which this is valid by x_- and x_+. All points outside this region have contributions to their density from the departing density in $-1 < \varepsilon < 1$ or the irregularly dispersing region $\mu_A - 1 < \varepsilon < \mu_A + 1$, thus introducing non time-invariant contributions (see the changing content of the dashed integration intervals in Figure 24).

Calculating the position of the plateau from the minimal and maximal allowed spacial coordinates at $\mu_B + 1$ and $\mu_A - 1$ yields

$$x_{+,-} = \frac{A}{2} \pm \frac{A}{2} \left(1 - \frac{4}{\mu_A - \mu_B} \right) \quad \text{for} \quad \mu_A - \mu_B \geq 4, \tag{8.15}$$

which is confirmed (up to small contributions from tunneling effects) by our simulations. The plateau region only exists for $\mu_A - \mu_B > 4$, thus for the situation shown in figures 23 and 24.For $\mu_A - \mu_B < 4$ the spatial ranges for escaping and dispersing particles superpose each other.

8.7 Oscillations

The second interesting feature of the dynamics we observe inside the linear potential region is a periodic exchange of density between the regions on the left and on the right side of the plateau, which can be interpreted as oscillations between two macroscopic localized states. The main dynamics is again caused by the uniform displacement of density inside the energy region $\mu_B + 1 < \varepsilon < \mu_A - 1$. Supplementary to this, we observe an additional oscillation of density for $x < x_-$ which is added to these main oscillations. These smaller contributions to the particle density are caused by the particles trapped inside the energy region $\mu_A - 1 < \varepsilon < \mu_A + 1$, which oscillate irregularly. In order to avoid this perturbation, one may let these blocked particles escape by opening a propagation band on the left by using a final potential of the form

$$\mu_i = \begin{cases} \mu_B & \text{for} \quad A \leq i < L \\ \mu_A - \frac{\mu_A - \mu_B}{A} i & \text{for} \quad 0 \leq i < A \; . \\ \mu_A & \text{for} \quad i \leq 0 \end{cases} \tag{8.16}$$

We will however leave the discussion of the behavior in this case for later.

8.7.1 Period

Let us estimate the period of the main movement by using the droplet-model. In analogy to the step system we can define a local velocity at a given position x depending on the energy ε and position:

$$v|_x = \sin(q)|_x = \pm\sqrt{1 - (\varepsilon - \mu(x))^2}.$$

The time of one period (the time for a droplet to travel from the left boundary to the right and back at this speed) is for any droplet and within the energy range $\mu_B + 1 < \varepsilon < \mu_A - 1$ independent from the actual energy value:

$$T = \oint \mathrm{d}x \frac{1}{v|_x} = 2 \frac{A}{\mu_A - \mu_B} \int_{-1}^{1} \frac{\mathrm{d}(\varepsilon - \mu(x))}{\sqrt{1 - (\varepsilon - \mu(x))^2}} = 2\pi \frac{A}{\mu_A - \mu_B} \tag{8.17}$$

This result (which is the main reason for the plateau we observed) is confirmed by Figure 23, because densities at times differing by T superpose. To verify our result we compare T to measurements of the period of oscillations for different potential slopes in Figure 25 again confirming our calculations.

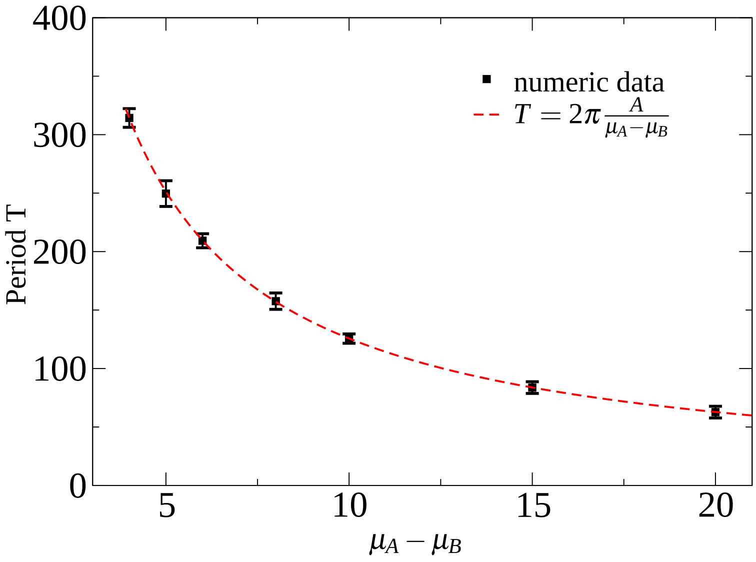

Figure 25: Period of the main oscillations in the trapping region of the linear potential for a system of $L = 1000$, $A = 200$. For $\mu_A - \mu_B$<4, these oscillations were not observed (no plateau).

8.7.2 Dynamics of an isolated Droplet

In the same way we can calculate the time-evolution of a single droplet of energy ε_s for $t > 0$: We assume that this single droplet has a position $x(t)$ with $x(0) = x_0$. Analogously to (8.17) using $\Delta = \mu_A - \mu_B$:

$$t = \int_{x0}^{x} \mathrm{d}x' \frac{1}{v|_{x'}} = \pm 2\frac{A}{\Delta} \int_{\varepsilon_s - \mu(x_0)}^{\varepsilon_s - \mu(x)} \frac{\mathrm{d}(\varepsilon_s - \mu(x'))}{\sqrt{1 - (\varepsilon_s - \mu(x'))^2}} = \pm 2\frac{A}{\Delta}(\arcsin(y) - \arcsin(y_0)), \quad (8.18)$$

The ± stands for the solution of particles initially moving to the right and left. We use the variable change $y = \varepsilon_s - \mu(x)$ for $x(t)$ and x_0. Inverting (8.18) then yields the fundamental relation for the displacement of a single droplet:

$$\varepsilon_s - \mu(x) = y = \sin(\arcsin(y_0) \mp t^*) \quad (8.19)$$

whith the rescaled time $t^* = t\frac{\Delta}{2A}$. As all of the droplets forming the total density move independently, we need only to identify the initial density at the initial position $\rho^0(y_0)$ corresponding to $\rho(y,t)$ where y_0 is given by (8.19). This can be formulated for any final value of y, by using the Dirac delta to choose the right initial position:

$$\rho(y,t) = \int_{-1}^{1} \mathrm{d}y_0 \, \rho^0(y_0) \delta(\sin(\arcsin(y_0) \mp t^*) - y)$$

The Dirac Delta can therefore be interpreted as the Greens function of a single particle displacement. Of course we can easily recover the dynamics in terms of x at a given energy, by undoing the change of variables $y = \varepsilon - \mu(x)$.

8.7.3 Semi-Classical Model for the Oscillation Dynamics

Let us push the model used a little further to model the full displacement of the particle density. First we calculate the initial density inside the new system associated to an infinitesimal energy interval $\rho^0(\tilde{y})$ using (8.11) yielding $\tilde{y} = -\cos(q)$.

Using (8.19) we can then calculate the displacement of this density over time for a given energy. We make the assumption that due to the thermal character of the initial state, there is no preferred initial direction such that we have for the initial density moving to the right and to the left $\rho_{\rightarrow}(\tilde{y}) = \rho_{\leftarrow}(\tilde{y}) = \frac{1}{2}\rho^0(\tilde{y})$.

We assume that the total density of particles is given at any point x by the superposition of all of the energy eigenstates, but we will limit our calculations to energies ε inside $\mu_B + 1 < \varepsilon < \mu_A - 1$. So the last step is to integrate for every position x the density over the allowed energy range.

$$\begin{aligned}
\rho(x,t) =& \int_{-1}^{1} \mathrm{d}y \sqcap \left(\frac{\mu_A}{A}x + 1 - \Delta \ldots \frac{\Delta}{A}x - 1; y \right) \rho(y,t) \\
=& \int_{-1}^{1} \mathrm{d}y \sqcap (\sim; y) \int_{-1}^{1} \mathrm{d}\tilde{y}\, \rho(\tilde{y}) \frac{\delta\Big(\sin(\arcsin(\tilde{y}) + t^*) - y \Big) + \delta\Big(\sin(\arcsin(\tilde{y}) - t^*) - y \Big)}{2} \\
=& \int_{-1}^{1} \mathrm{d}y \sqcap (\sim; y) \\
& \quad \int_{0}^{\pi} \mathrm{d}q \frac{\sqcap(0 \ldots q_N; q)}{2\pi} \left(\delta\Big(\sin(-t^* + \frac{\pi}{2} - q) - y \Big) + \delta\Big(\sin(+t^* + \frac{\pi}{2} - q) - y \Big) \right) \\
=& \frac{1}{2\pi} \int_{t^* - q_N}^{t^* + q_N} \mathrm{d}q^* \sqcap \left(\frac{\Delta}{A}x + 1 - \Delta \ldots \frac{\Delta}{A}x - 1; -\cos(-q^*) \right)
\end{aligned} \tag{8.20}$$

This integral can be done for any given value of x and t. The integration surface is sketched in Figure 26.

Inside $\frac{A}{2} \pm \frac{A}{2}\left(1 - \frac{4}{\Delta}\right)$ for $\Delta \geq 4$ the plateau is reproduced, because the door function is always one:

$$\rho(x,t^*) = \frac{2q_N}{2\pi} = \frac{q_N}{\pi} = \rho_0$$

For $t^* = 2n\pi$ we get

$$\begin{aligned}
\rho(x,t^*) =& \quad \sqcap \left(0 \ldots \frac{A}{\Delta}(1 - \cos(q_N)); x \right) \frac{\arccos(1 - \frac{\Delta}{A}x)}{\pi} \\
& + \sqcap \left(\frac{A}{\Delta}(1 - \cos(q_N)) \ldots \frac{A}{\Delta}(\Delta - 2); x \right) \frac{q_N}{\pi} \\
& + \sqcap \left(\frac{A}{\Delta}(\Delta - 2) \ldots \frac{A}{\Delta}(\Delta - 1 - \cos(q_N)); x \right) \frac{q_N - \arccos(1 - \frac{\Delta}{A}x)}{\pi}.
\end{aligned} \tag{8.21}$$

The case $t^* = (2n+1)\pi$ is then easy to establish by simply using the mirror symmetry at $\frac{A}{2}$ and setting $x' = A - x$ in (8.21).

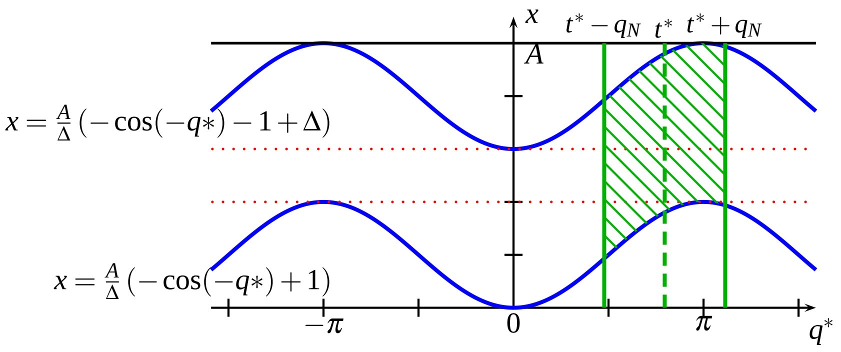

Figure 26: Integration range of (8.20). Over time the range $q^* = t^* - q_N \dots t^* + q_N$ shifts along with t^*. The integration is carried over q^* inside the surface limited by the solid blue curves and the extremal values of q^*. As an example, the surface for $t^* = 3.5$ is hatched in green. The dotted red lines mark the boundary of the plateau region.

For $t^* = \frac{\pi}{2} + n\pi$ we get

$$\begin{aligned}
\rho(x,t^*) =& \sqcap\left(\frac{A}{\Delta}(1-\sin(q_N))\dots\frac{A}{\Delta}(1+\sin(q_N));x\right)\frac{q_N + \arcsin(\frac{\Delta}{A}x-1)}{2\pi}\\
&+\sqcap\left(\frac{A}{\Delta}(1+\sin(q_N))\dots\frac{A}{\Delta}(\Delta-1-\sin(q_N));x\right)\frac{q_N}{\pi}\\
&+\sqcap\left(\frac{A}{\Delta}(\Delta-1-\sin(q_N))\dots\frac{A}{\Delta}(\Delta-1+\sin(q_N));x\right)\frac{q_N + \arcsin((\Delta-1-x)\frac{\Delta}{A})}{2\pi}
\end{aligned}$$

The results are shown in Figure 27 for the system we were treating so far, but also for a system with an initial density developing under a potential allowing high energy modes to escape as given by (8.16). This not only shows a very good agreement to the calculated profiles, but also, that the additional density we see on the left of the plateau is really due to the particles in the high energy levels of $\omega > \mu_A + 1$. A comparison of these density profiles would therefore be a good starting point to analyze the behavior of these particle modes.

8.8 Current

From what we have seen so far we expect a current of particles to flow back and forth through the plateau region and generating the oscillations between the two macroscopic states we identified for the energy range $\mu_B + < \varepsilon < \mu_A - 1$. This current should be spatially constant within the plateau region and periodic with period T in time.

We can define a local current j associated to each connection $i = 0 \dots L-2$ between neighboring sites $i, i+1$ by using

$$\frac{\mathrm{d}\,\mathbf{n}_i}{\mathrm{d}t} = \mathbf{j}_i - \mathbf{j}_{i+1} = \mathrm{i}\,[\mathbf{H},\mathbf{n_i}] = \mathrm{i}\left[\omega\sum_i \mathbf{c}_i^+\mathbf{c}_{i+1} + \mathbf{c}_{i+1}^+\mathbf{c}_i, \mathbf{c}_i^+\mathbf{c}^i\right]$$

and identifying the terms consisting of operators acting on $i, i+1$ and $i+1, i+2$ (c.f. [14]).

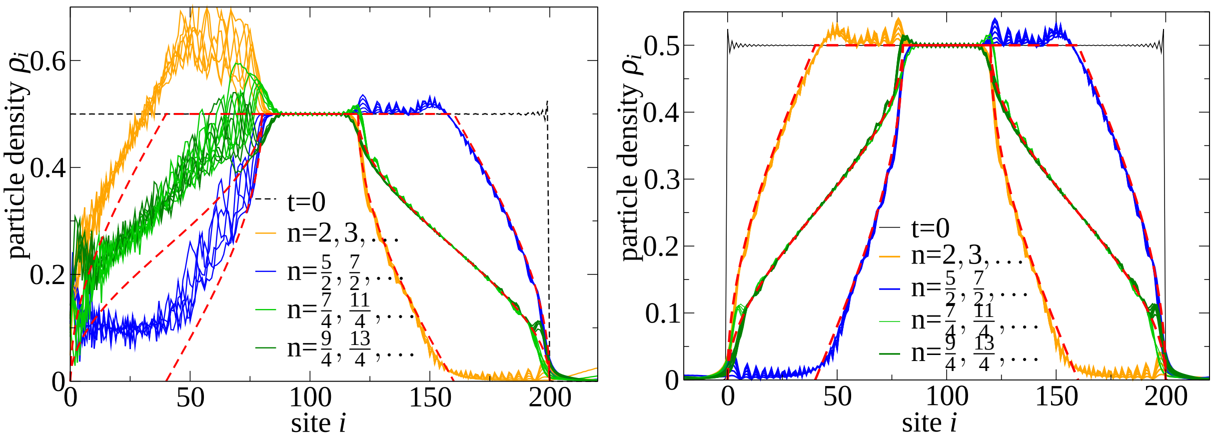

(a) Progative System to teh right

(b) Propagative System to the left and right

Figure 27: $\mu_A - \mu_B = 5$,$L = 1000$,$A = 200$. The curves represent different times $t = 2\pi\frac{A}{\mu_A-\mu_B}n$. Left: The situation of a system allowing escape only to the right. Right: System allowing escape to the left also. The dashed curves represent the density calculated for these times from (8.20)

Transforming to Clifford operators then yields

$$\mathbf{j}_i = \mathrm{i}\frac{1}{4}\left[\Gamma^2_{i+1}\Gamma^2_i + \Gamma^1_{i+1}\Gamma^1_i\right]. \tag{8.22}$$

The expectation value of the currents can thus at any time be calculated as the off-diagonal elements of the correlation matrix $\hat{\mathbf{G}}(t)$ given by (4.6).

Numeric results for the current in the middle of the plateau at $\frac{A}{2}$ as a function of time are given in Figure 28a. We expect the exchange of particles and thus the current between the two localized states we were treating in the previous chapter to be of period $T = 2\pi\frac{A}{\mu_A}$ if the slope of the potential is high enough to create a plateau. Otherwise we have contributions from high-energy states and departing particles.

We will again use the classical model introduced in 8.7.3 to reproduce this behavior for the states with energies $\mu_A - 1 > \varepsilon > \mu_B + 1$. The velocity is $v(y) = \pm\sin(\arccos(-y)) = \pm\sin(q)$. We make the assumption, that the current is analog to a classical current given by $\rho(y,t)v(y)$ and that the total current then is the superposition of all of these currents at a given position. Therefore (with $t^* = \frac{tA}{\Delta}$)

$$\begin{aligned}
j(x,t^*) =& \int_{-1}^{1} \mathrm{d}y \sqcap\left(\frac{\mu_A}{A}x + 1 - \Delta \ldots \frac{\Delta}{A}x - 1; y\right)\rho(y,t)v(y) \\
=& \int_{-1}^{1} \mathrm{d}y \sqcap(\sim; y)\left|\sin(\arccos(-y))\right| \\
& \int_0^{\pi} \mathrm{d}q \frac{\sqcap(0\ldots q_N; q)}{2\pi}\left(\delta\left(\sin(-t^* + \frac{\pi}{2} - q) - y\right) - \delta\left(+\sin(t^* + \frac{\pi}{2} - q) - y\right)\right) \\
=& \frac{1}{2\pi}\int_{t^*-q_N}^{t^*+q_N} \mathrm{d}q^* \sqcap\left(\frac{\Delta}{A}x + 1 - \Delta \ldots \frac{\Delta}{A}x - 1; -\cos(-q^*)\right)\sin(-q^*)
\end{aligned} \tag{8.23}$$

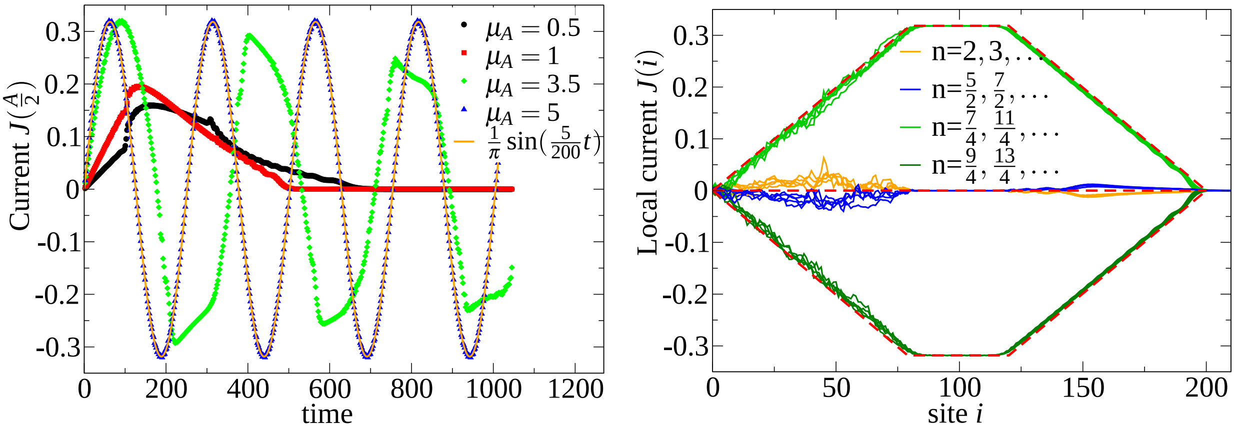

(a) Current inside the plateau region

(b) Local current

Figure 28: Current in a system of $L = 1000, A = 200$ created with half filling at $t = 0$. Left: Current as a function of time in the middle of the linear region ($x = \frac{A}{2}$) for different μ_A. The theoretical curve has been created using the result from (8.24). For $\mu_A \leq 1$ we see the departure of particles as the dominating element while for $\mu_A = 5$ the oscillation dominates the picture. Right: profile of the local current density for different times $t = \frac{2\pi A}{\mu_A - \mu_B} n$ and the dashed theoretical curves.

.

We proceed to solve this for some special cases. Inside the plateau region ($\Delta \geq 4$):

$$j(x,t^*) = \frac{1}{2\pi}\int_{t^*-q_N}^{t^*+q_N} \mathrm{d}q^* \sin(-q^*) = \frac{1}{\pi}\sin(q_N)\sin(t^*) \tag{8.24}$$

Note that there is a maximum particle exchange for half filling, while we have no exchange for $q_N = 0, \pi$ (completely filled or completely empty). The observation of perfect sinus inside the plateau region supports the thesis to have the oscillatory exchange of particles between two localized macroscopic states.

This result is shown in Figure 28a and reproduces very well the numeric data. Furthermore, $t^* = \frac{\pi}{2} + 2n\pi$ yields the simple result (a simple trapezoid)

$$\begin{aligned} j(x,\frac{\pi}{2}) &= \frac{1}{2\pi}\int_{\frac{\pi}{2}-q_N}^{\frac{\pi}{2}+q_N} \mathrm{d}q^* \sqcap\left(\frac{\Delta}{A}x + 1 - \Delta \dots \frac{\Delta}{A}x - 1; \cos(-q^*)\right)\sin(-q^*) \qquad (8.25)\\ &= \sqcap\left(\frac{A}{\Delta}(1-\sin(q_N))\dots\frac{A}{\Delta}(1+\sin(q_N));x\right)\frac{\frac{\Delta}{A}x - 1 - \sin(q_N)}{2\pi} \\ &\quad + \sqcap\left(\frac{A}{\Delta}(1+\sin(q_N))\dots\frac{A}{\Delta}(\Delta-1-\sin(q_N));x\right)\frac{\sin(q_N)}{\pi} \\ &\quad + \sqcap\left(\frac{A}{\Delta}(\Delta-1-\sin(q_N))\dots\frac{A}{\Delta}(\Delta-1+\sin(q_N));x\right)\frac{\frac{\Delta}{A}(\Delta-1-x)+\sin(q_N)}{2\pi}. \end{aligned}$$

This result is shown in Figure 28b alongside the numerical results. We see very small distorsions of the theretical trapezoid solution due to the not exactly flat initial filling (c.f. Figure 3).

Part III

Conclusion and Outlook

9 Conclusion

We have shown in close connection between theoretical developments and numerical simulations, the main features of the quench dynamics for the Bose-Hubbard-Hamiltonian in the case of a step and a linear final potential. The properties of a localized initial state at $T = 0$ have been presented as well as conserved quantities of the system.

For the case of a step potential and a linear potential, which are applied as sudden quench to this initial state, we have established the diagonalized Hamiltonian and analyzed its energy spectrum.

First we investigated the time-evolution in the case of the step potential. This lead to the counterintuitive result of particles being trapped inside their initial spacial region, although a classical approach would predict the quench potential at $t > 0$ to be repulsive there. This behavior was reproduced analytically using a continuum limit approach.

For the case of a linear potential, this trapping of particles persisted and was modeled using a similar approach. Additionally we analyzed the dynamics of these trapped particles. The dynamics can best be interpreted as the oscillation of density between two localized macroscopic states in the left and to the right part of the trapping region. These oscillations of density were modeled using a semi-classical approach allowing us to identify its macroscopic basis states.

The good agreement with the numerical simulations suggest that we have achieved a good understanding of the underlying principles and phenomena governing this quench dynamics, which presents us with a good starting point for further research.

10 Further Research and possible Generalizations

The model we used allows for a series of generalizations and further development. First of all it should be possible to use it for predictions about the behavior of the high-energy modes, we treated only phenomenologically. On the formal side, it should then be possible to generalize the techniques used to many other forms of potentials analog to what we show in appendix A. This should allow to model the departure dynamics and even the time-evolution in the semi-classic model for more complicated potentials.

Furthermore, the persistence of these trapping and oscillatory phenomena can be studied if weakening the hypothesis of a hard-core boson-boson interaction. This is actually been done in my research group in parallel to this work using DMRG. Although the results are still to be verified we see hints to a changing behavior at high fillings and for the blocking dynamics.

For applications, refined calculations for different potentials and their reproducibility in experiments could be done. This might yield a protocol for a “self-compression” of bosonic condensates, because the particles in the high energy levels cause the density to be locally higher than the initial density, when the oscillating density is localized in the left macroscopic state.

Part IV

Appendix

A Calculation of the Density of States in the Generalized Case

Here we want to generalize the technique used in 8.2 to calculate the density of states for classes of different potentials.

For system B system, we assume the flat potential and thus we have

$$n(\varepsilon)_B = \frac{n(q_B)}{\sqrt{1-(-\mu_B+\varepsilon)^2}}.$$

As this is well understood and only adds to the contribution of the left system, we can now treat the right left system independently.

We again cut system A into infinitesimal small intervals dx and integrate the local densities of state for a given energy value. In analogy with the results in the step potential (7.5) we define the local density of states as

$$n(\varepsilon, x) = \frac{\prod(\mu(x)-1\ldots\mu(x)+1;\varepsilon)}{\pi\sqrt{1-(\varepsilon-\mu(x))^2}},$$

where the spatial dependency is solely carried by the explicitly x-dependent chemical potential.

Now we integrate to get (for $0 < x < A$ and a potential for which $\frac{\mathrm{d}\,\mu(x)}{\mathrm{d}\times} \leq 0$)

$$\begin{aligned}
n(\varepsilon) &= \int_0^A \mathrm{d}x\, n(\varepsilon, x) = \frac{\prod(\mu_A(x)-1\ldots\mu_A(x)+1;\varepsilon)}{\pi\sqrt{1-(\varepsilon-\mu(x))^2}} \\
&= \int_{\max(-1,\varepsilon-\mu_A)}^{\min(1,\varepsilon-\mu_B)} \mathrm{d}(\varepsilon-\mu(x)) \left(\frac{\mathrm{d}\,x}{\mathrm{d}(\varepsilon-\mu(x))}\right) \frac{1}{\pi\sqrt{1-(\mu_A(x)-\varepsilon)^2}} \\
&= \int_{\max(-1,\varepsilon-\mu_A)}^{\min(1,\varepsilon-\mu_B)} \mathrm{d}y \left(\frac{\mathrm{d}\,x}{\mathrm{d}(\varepsilon-\mu(x))}\right) \frac{1}{\pi\sqrt{1-(y)^2}}
\end{aligned} \tag{A.1}$$

A special case is the step potential itself. In this case the derivative vanishes and we obtain a Dirac delta function $(\mu_A - \mu_B)\delta(x-A)$ reproducing the result we postulated.

The same calculations can be done for a potential of ($\frac{\mathrm{d}\,\mu(x)}{\mathrm{d}\times} \geq 0$), which will invert the minimum and maximum for the borders and ad a negative sign. Potentials changing their monotony behavior can also be calculated by taking into account the different permitted and non-permitted regions.

Let us calculate the explicit result for a group of simple potentials.

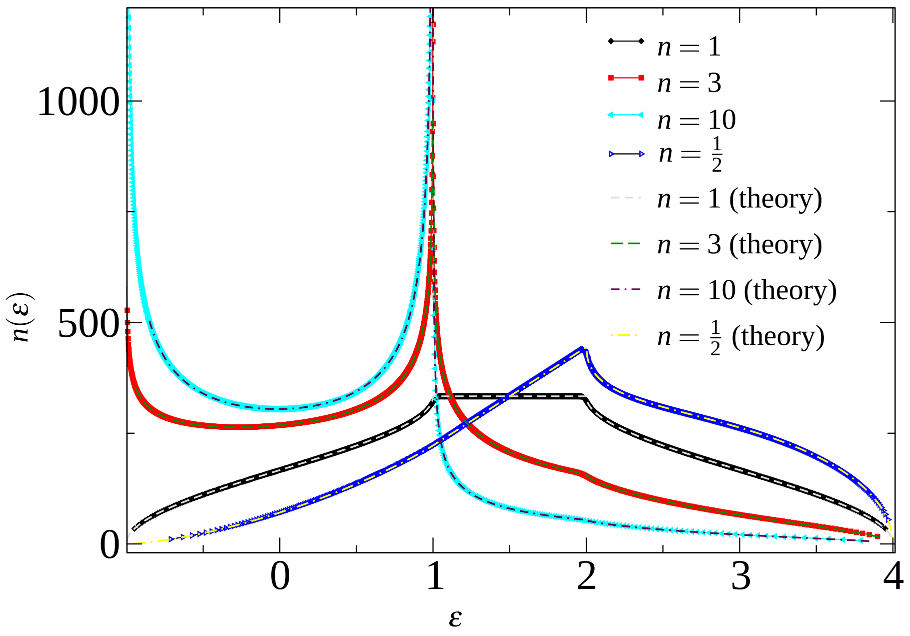

Figure 29: Comparison of theoretical (lines) and simulation results (points) for potentials of the form $\mu(x)=\mu_A\frac{(A-x)^n}{A^n}$ with $A=1000$ and $\mu_A=3$

For the case of a potential of the form $\mu(x)=\mu_A\frac{(A-x)^n}{A^n}$ we get:

$$\left(\frac{\mathrm{d}\,x}{\mathrm{d}(\varepsilon-\mu(x))}\right)=\frac{A}{\mu_A^{\frac{1}{n}}n}(\varepsilon-y)^{\frac{1}{n}-1}\quad y=\varepsilon-\mu(x)$$

Into this form we can easily include a nonzero value for μ_B by shifting the energy spectrum without any further calculations.

The resulting integrals can be solved and but give rise to complicated hypergeometric functions. For the special case $n=1$ we recover the results for the linear potential. We give a couple of examples how these solutions will look like and compare them to our numerical data in 29.

Considering the excellent agreement between the calculated and simulated results, we can assume our calculations as a good starting point for further calculations like the departure probability.

B Informatics System and Simulation Routine used

The calculations accompanying our project were performed in C++ making use of the GNU Scientific Libraries originally written for C. The procedure of calculation corresponds largely to the mathematical procedure mentioned in the introduction. A speed benchmark which gives an idea of the time-consumption involved, showed that the running time scales approximately like $T=N_{steps}L^{2.8}T_0$, where L is the system size and N_{steps} the number of time-points calculated. T_0 is a reference time, which largely depends on the processing system used, being of order 10^{-6}s.

C Acknowledgements

I want to thank the whole statistical physics group in Nancy for very interesting discussions, instructive advice and an always wide-open door. My special thanks in this regard go to my advisor Dragi Karevski and to Xavier Durang. I would also like to thank visiting Prof. Moo Young Choi for agreeing to be a member of the examining commitee as well as Prof. Malte Henkel. Furthermore, i want to thank the organizers of the Saar-Lor-Lux program for their support throughout my whole studies on the administrative level.

References

[1] Milton Abramowitz and Irene A. Stegun. *Handbook of Mathematical Functions with Formulas, Graphs, and Mathematical Tables*. Dover, New York, ninth dover printing, tenth gpo printing edition, 1964.

[2] T. Antal, Z. Rácz, A. Rákos, and G. M. Schütz. Transport in the *xx* chain at zero temperature: Emergence of flat magnetization profiles. *Phys. Rev. E*, 59(5):4912–4918, May 1999.

[3] Ghassan George Batrouni, Richard T. Scalettar, and Gergely T. Zimanyi. Quantum critical phenomena in one-dimensional bose systems. *Phys. Rev. Lett.*, 65(14):1765–1768, Oct 1990.

[4] Edgar Fieberg. *Das intuitive Wissen über Bewegungsgesetze*. Waxmann Verlag, 1998.

[5] Matthew P. A. Fisher, Peter B. Weichman, G. Grinstein, and Daniel S. Fisher. Boson localization and the superfluid-insulator transition. *Phys. Rev. B*, 40(1):546–570, Jul 1989.

[6] M. Giradeau. Relationship between systems of impenetrable bosons and fermions in one dimension. *Journal of Math. Physics*, 1(6), 1960.

[7] Markus Greiner, Olaf Mandel, Tilman Esslinger, Theodor Hänsch, and Immanuel Bloch. Quantum phase transition from a superfluid to a mott-insulator in a gas of ultracold atoms. *Nature*, 415(13), 2002.

[8] J. Hubbard. Electron correlations in narrow energy bands. *Proc. Roy. Soc.*, 276, 1963.

[9] D. Jaksch, C. Bruder, J. I. Cirac, C. W. Gardiner, and P. Zoller. Cold bosonic atoms in optical lattices. *Physical Review Letters*, 81:3108, 1998.

[10] Dragi Karevski. Ising quantum chains. arXiv No. 0611327, November 2006.

[11] C. Kollath, U. Schollwöck, J. von Delft, and W. Zwerger. One-dimensional density waves of ultracold bosons in an optical lattice. *Phys. Rev. A*, 71(5):053606, May 2005.

[12] Elliott Lieb, Theodore Schultz, and Daniel Mattis. Two soluble models of an antiferromagnetic chain. *Annals of Physics*, 16(3):407–466, 1961.

[13] D. S. Petrov, G. V. Shlyapnikov, and J. T. M. Walraven. Regimes of quantum degeneracy in trapped 1d gases. *Phys. Rev. Lett.*, 85(18):3745–3749, Oct 2000.

[14] T. Platini, R. J. Harris, and D. Karevski. Fourier's law on a one-dimensional optical random lattice. *Mathematical Systems Theory*, 43:135003, 2010.

[15] Thierry Platini. *Chaînes de spins quantiques hors de l'équilibre*. PhD thesis, UHP Nancy, 2008.

[16] Thierry Platini and Dragi Karevski. Scaling and front dynamics in ising quantum chains, 2005.

[17] Thierry Platini and Dragi Karevski. Relaxation in the xx quantum chain, 2006.

[18] O. Romero-Isert, K. Eckert, C. Rodom, and A. Sanpera. Transport and entanglement generation in the bose–hubbard modeeckert k. *Journal of Physics A*, 40, 2007.

[19] Subir Sachdev. *Quantum Phase Transitions*. Cambridge University Press, 1999.

[20] Niklas Teichmann, Dennis Hinrichs, Martin Holthaus, and Andre Eckardt. Bose-hubbard phase diagram with arbitrary integer filling. *Phys. Rev. B*, 79:100503, 2009.

[21] H. S. J. van der Zant, F. C. Fritschy, W. J. Elion, L. J. Geerligs, and J. E. Mooij. Field-induced superconductor-to-insulator transitions in josephson-junction arrays. *Phys. Rev. Lett.*, 69(20):2971–2974, Nov 1992.